Mesogranulation in the quiet Sun

MAS8091: MMath Project

School of Mathematics & Statistics

Martin Chambers

Supervisor: Paul Bushby

Abstract

The central object in our solar system is the Sun. However, a lot is still not understood about convective processes within the sun. Mesogranulation is a theorised scale of convection lying between granulation and supergranulation. Since its discovery in 1981 by November & Simon its existence has been intensely debated within the solar community. Many researchers, using a number of different methods, have discovered a wide range of results. One of the main techniques used to study the solar photosphere are tracking algorithms. The validity of tracking algorithms is often questioned, with many researchers suggesting that the discovery of mesogranulation was down to averaging processes in the algorithms. Thus, I am going to study a simple model of convection within a box in an attempt to answer two major questions: Does mesogranulation exist?; are tracking algorithms a good method to pick out such a scale?

Acknowledgements

I would like to thank Paul Bushby for his unending support and enthusiasm during this project. Secondly, I would like to acknowledge that without the support of Catherine Lack, I would not be where I am today.

Contents

1. Introduction

The solar interior is built up of four layers defined by the different processes that occur there. The innermost region of the Sun is the core in which energy is created via nuclear fusion. This energy is forced outwards into the above layer; the radiative zone. Here, via a random walk, radiation is transported to the next layer. This layer is called the tachocline and is a very thin layer between the relatively calm radiative zone and unstable solar convection zone. In the solar convection zone material moves by convection and the fluid motions are visible at the surface as granules and supergranules. The solar convection zone is an area of the Sun highly studied, but with a lot of questions left unanswered. The solar interior is shown pictorially in Figure 1.1.

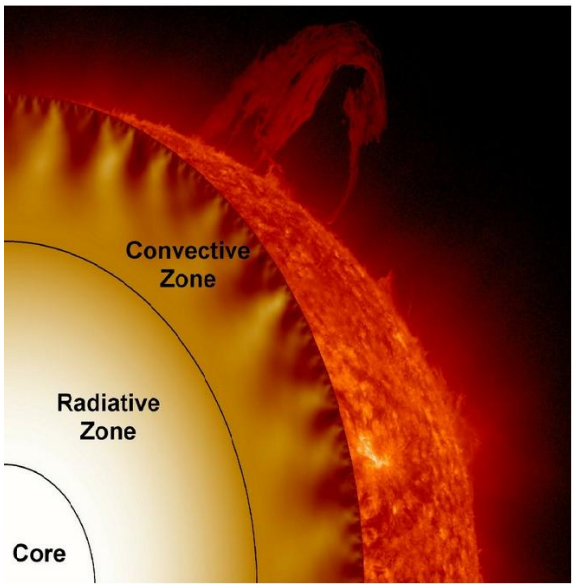

Figure 1.1: A diagram depicting the main layers within the sun. Reference: solarscience.msfc.nasa.gov/interior.shtml

Granules are a cellular like pattern that cover the surface of the Sun. They occur naturally as a result of Rayleigh-Bénard convection, that is, a layer of fluid heated from below develops a regular pattern of convective cells. The heated plasma rises, spreads out, cools, and then descends down intergranular lanes. It is this strong cooling of the Sun's surface that drives solar convection. In the Sun this pattern is called granulation. The image in Figure 1.2 illustrates this. They are notably the most understood flow within the solar convection zone, being well reproduced in numerical simulations and having many studies dedicated to them. A typical granule is ≈ 1 Mm across, where 'Mm' represents a megametre (1000 Km), and have an average lifetime of ≈ 10 minutes (Title et al. 1989). Supergranules are a much larger scale motion superimposed upon granulation with an approximate size of 30 Mm across and a lifetime of several days. These fluid motions are illustrated in Figure 1.3.

This brings us to mesogranulation. It is a theorised scale thought to occur in be-

tween granulation and supergranulation. It was first discovered by November and Simon (1981) who noticed prominent vertical motions at scales of size $\approx 5-7$ Mm. Mesogranulation has been measured many times by a range of researchers: Ginet and Simon (1992), Chou et al (1992), Abdussamatov (1993) etc. However, its existence is of intense debate within the solar community. November (1994) suggested that the term mesogranulation was misleading and that it was merely the "vertical component of supergranular convection". Strauss and Bonaccini (1997) stated that mesogranulation was a more powerful extension of granulation. In addition, other researchers found no conclusive evidence in the power spectrum at scales that would correspond to mesogranulation (Wang 1989; Chou et al. 1991; Strauss et al. 1992). Even those who have detected mesogranulation differ in their measurements of lifetime and size.

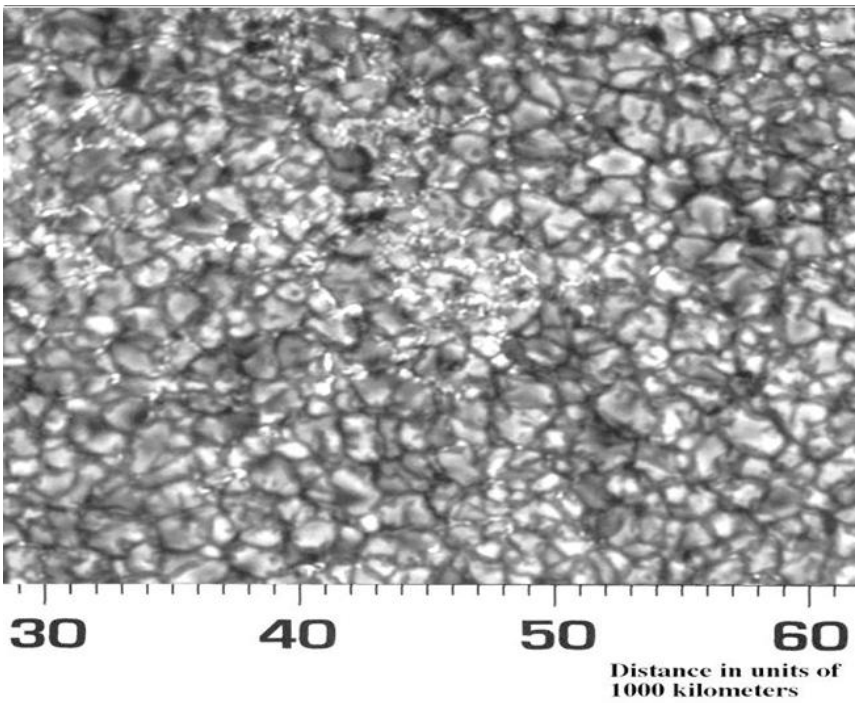

Figure 1.2: This image was taken from the Swedish Vaccuum Solar Telescope and shows granulation on the surface of the Sun. Reference: solarscience.msfc.nasa.gov/feature1.shtml

There are many methods implemented by previous researchers that have been used to study the fluid motions at the surface of the solar convection zone. November and Simon (1981) are considered to be the fathers of the most common method: tracking algorithms. This method has been criticised as it is suggested that mesogranulation is produced as an artefact of the algorithm (Roudier et al. 1999b; Rieutord et al. 2000). A simple model was created by Matloch et al. (2009) which showed that mesogranules were created by "weird consequences of averaging processes". Consequently, in order to prove mesogranulation exists, either correlation tracking algorithms will need to be validated or a different technique used to detect mesogranulation.

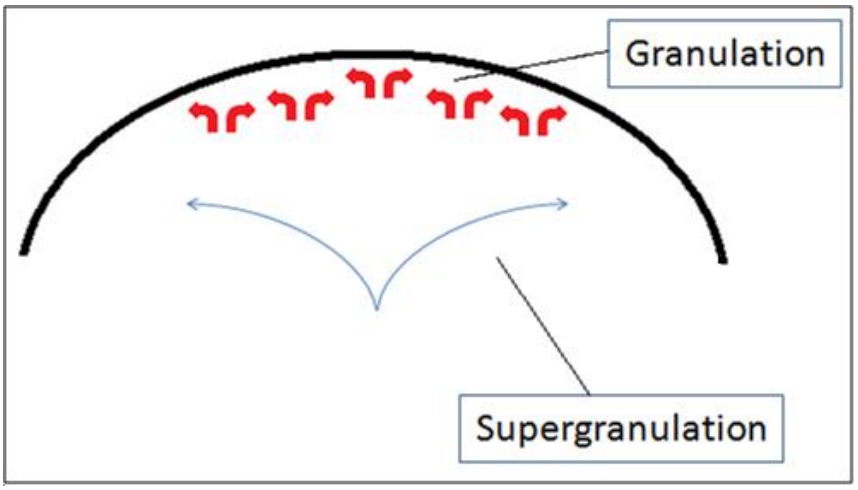

Figure 1.3: A simple background on the convective processes that are occurring in the solar convection zone. Granulation is the small scale flow near the surface. Supergranulation is the larger scale flow.

In the solar convection zone, the overturning eddies tend to expel magnetic flux (Weiss 1966). This magnetic flux exits from the granule interior and becomes concentrated as localised structures within the intergranular lanes (Lin & Rimmele 1999). This is a small scale dynamo mechanism that requires only the chaotic motions of solar convection. Therefore, it is unsurprising that local convective motions can influence the magnetic field. Many observations have suggested that mesogranular cells expel a concentration of magnetic flux that accumulates preferentially at the boundary (Cerdena 2003; de Wijn et al. 2005; Chaouche et al. 2011). Therefore, if a scale in between granulation and supergranulation exists, then the magnetic field distribution may help identify it.

In chapter 2, I will go into more detail about compressible convection and the governing equations in the model. Then, I will perform a power spectrum analysis to see if there is evidence of mesogranulation in the flow. In chapter 4, I will present an in-depth write up of the tracking algorithm. Chapter 5 will display and examine the results of the algorithm. Finally, chapter 6 describes my discussions and conclusions.

2. Compressible convection

Convection within the Sun is of enormous importance, defining its internal structure and impacting upon all of the behaviour at and above the solar surface. Therefore, the aim of my dissertation is to investigate a basic model of convection. I wish to answer the question of whether mesogranulation is present within the fluid and determine if computational algorithms are a good method to detect its presence. Furthermore, by applying these methods to a basic model I hope to provide a stepping stone that will pave the way for similar results in more complex models.

Many recent studies of convection have had one central idea: Cartesian models of Boussinesq convection, in an electrically-conducting fluid are capable of producing a dynamo which is similar qualitatively to that observed in the solar photosphere (Cattaneo 1999; Cattaneo, Emonet, Weiss 2003). This Boussinesq approach has one main limitation: it ignores the effects of compressibility, which, as observations have shown us, is important in the solar convection zone. Several recent studies have tried to fix this problem by creating models based on compressible convection that incorporate as many of the relevant physical processes that occur within the Sun as possible (Rincon, Lignières, Rieutord 2005; Vögler & Schüssler 2007). Although, compressible convection models are much more complex numerically than Bousinesq models recent studies have shown it is possible to create convectively driven dynamo action within a layer of fluid. However, as many of the previous compressible convection models have been carried out in small computational domains, they were not able to investigate scales larger than granulation.

2.1 The simulation

I am going to study the evolution of an electrically-conducting, compressible fluid heated from below. The simulation data is taken from Bushby & Favier (2014) and is based on solving fully compressible convection within a box. It is a simple idealised portrayal of convection aimed at mirroring the flow within a region close to the surface of the quiet Sun.

The box itself is a Cartesian domain (x, y, z) of dimensions $0 \leq x, y \leq \lambda$ and $0 \leq z \leq 1$. There are two different data sets. For data set 1, $\lambda = 20$ Mm and any magnetic elements have been ignored. This means that the box for data set 1 is 20 Mm by 20 Mm by 1 Mm. For data set 2, $\lambda = 10$ Mm and a magnetic field has been introduced. Hence, both models are large enough to analyse behaviour at scales larger than granulation. The z-axis points vertically downwards, parallel to the constant gravitational acceleration, $\mathbf{g} = g\hat{\mathbf{z}}$, which implies that $z = 0$ and $z = 1$ correspond to the top and bottom of the box, respectively. Furthermore, the sides of the box are horizontally periodic meaning that if fluid exits through any side of the box it will enter through the side opposite to it. The top and bottom of the box are impermeable and stress-free meaning that fluid cannot leave through either surface and no stress forces exist at those boundaries.

To initialise the hydrodynamic simulation, a small random perturbation to the temperature distribution is imposed. Hence, the box is heated from below, with the top and bottom of the box held at fixed uniform temperatures. Finally, a seed magnetic field is introduced to the flow to initialise dynamo action. A basic illustration of the box that highlights the concept of the model is shown in Figure 2.1.

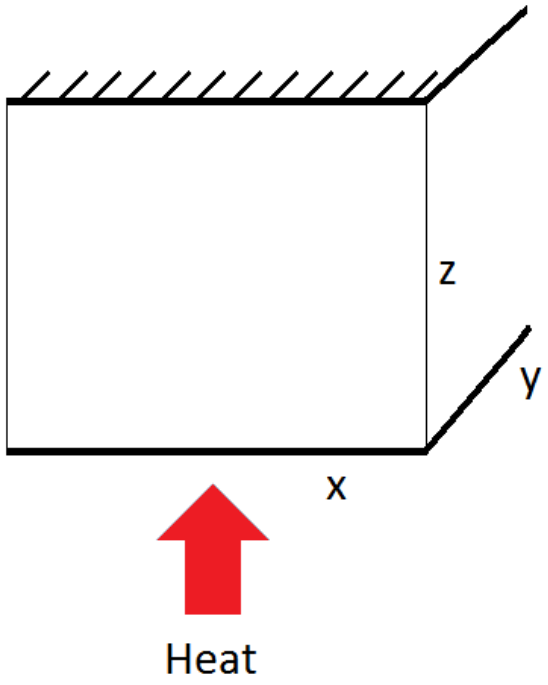

Figure 2.1: A diagram to graphically represent the simulation. The top and bottom of the box are impermeable ($u_z = 0$) and stress-free ($\partial u_x/\partial z = \partial u_y/\partial z = 0$). Both the top and bottom have fixed uniform temperatures, T_0 and $T_0 + \Delta T$ respectively, with $\Delta T \geq 0$. The sides of the box are horizontally periodic ($f(x + \lambda, y + \lambda, z, t) = f(x, y, z, t)$).

I have plotted the temperature map at four different depths within the box, shown in Figure 2.2. The plot exhibits a similar behaviour to the Sun's solar surface, where we also see a well defined granular pattern just below the surface ($z = 0.2$), defined by warm upflows and a surrounding network of cooler downflows. Similarly, the lower depths show behaviour similar to the solar convection zone, where the well defined granular patterns become weaker, less defined and the scales become larger. Therefore, although this is a simplistic model, the results from the simulation can be related in a qualitative way to the solar photosphere.

It should be noted that, although, the model can be related quantatitvely to the solar photosphere, it has one main drawback. Computational constraints mean that we can only model scales slightly larger than granulation. Therefore, we have no idea how larger scales such as supergranulation will impact upon the flow.

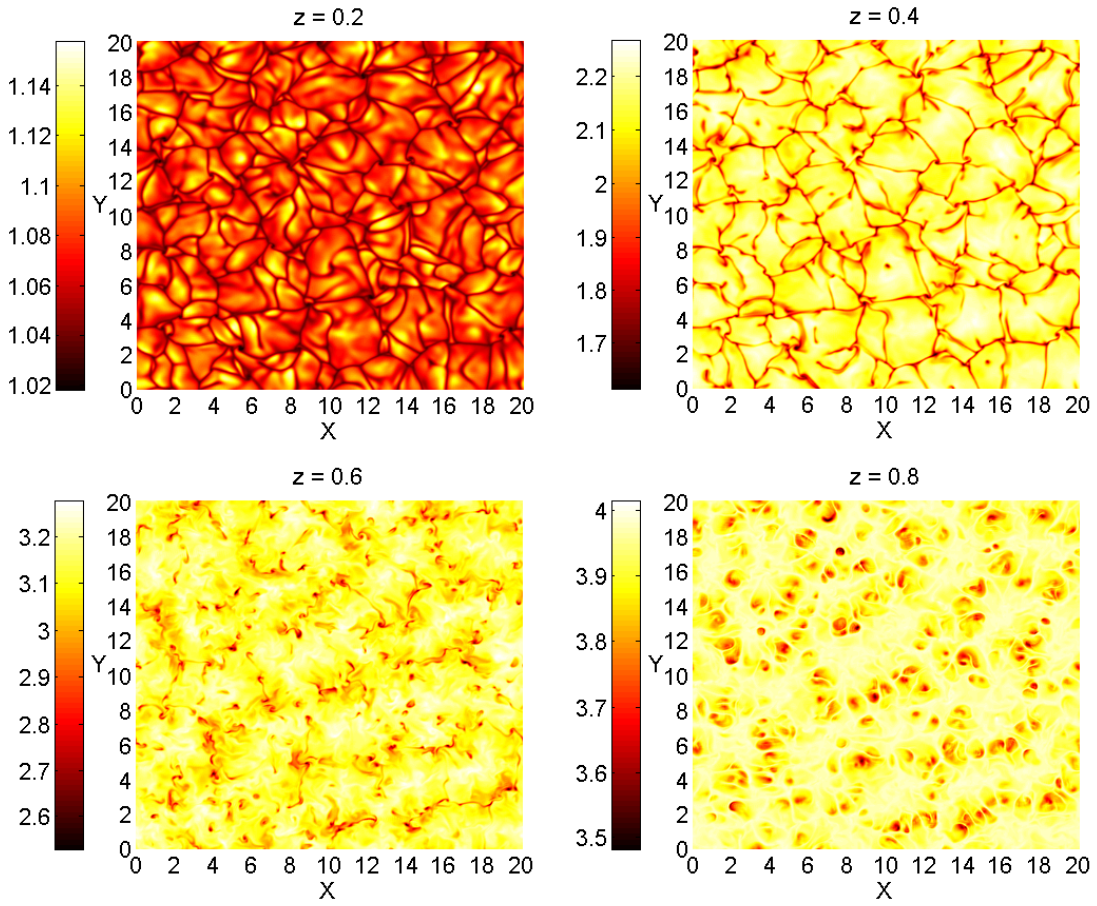

Figure 2.2: The temperature map for data set 1 at four different depths for time 1. The top left image shows the evolution of the fluid just below the surface. The temperature maps in the top right and bottom left show depths $z = 0.4$ and $z = 0.6$, respectively. The bottom right shows the fluid just above the bottom.

2.2 The governing equations

The properties of the fluid are described by many variables such as thermal diffusivity, K, the magnetic diffusivity, η, the magnetic permeability, μ_0 and the shear viscosity, μ. The unperturbed uniform, density at the upper surface is defined to be ρ_0, when there is no motion. In addition, specific heat capacities at constant density and pressure are added; c_v and c_p, respectively. We can use these to define the gas constant as $R_* = c_p - c_v$, whilst $\gamma = c_p/c_v$. For all of these quantities, we assume that they are constant throughout the fluid. The various parameters in the governing equations are described in detail in section 2.3. The governing equations follow Bushby & Favier (2014):

Under the above assumptions for the box and the fluid there are four governing equations for the density $\rho(\mathbf{x}, t)$, the fluid velocity $\mathbf{u}(\mathbf{x}, t)$, the magnetic field $\mathbf{B}(\mathbf{x}, t)$ and the temperature $T(\mathbf{x}, t)$. Let us start by defining the governing equation for density. First, note that we can use conservation of mass, so that the density $\rho(\mathbf{x}, t)$

satisfies

$$\frac{\partial \rho}{\partial t} + \nabla \cdot (\rho \mathbf{u}) = 0$$

for a fluid with velocity field $\mathbf{u}(\mathbf{x}, t)$. Expanding this out using the product rule, we obtain

$$\frac{\partial \rho}{\partial t} + (\mathbf{u} \cdot \nabla)\rho + \rho \nabla \cdot \mathbf{u} = 0. \tag{2.1}$$

The governing equation for the density is described by two terms. The first term, $\mathbf{u} \cdot \nabla \rho$, describes the changes in the density as material elements move from one point to another whilst, $\rho \nabla \cdot \mathbf{u}$ is proportional to the divergence of the flow velocity.

Next, we derive the governing equation for momentum. This is complex due to the fact that if we consider a blob of fluid, its momentum may change because of surface and body forces. Therefore, let us first consider the surface force for the fluid. In tensorial form the surface force is

$$\sigma_{ij} = -P(\mathbf{x}, t)\delta_{ij} + \mu \tau_{ij},$$

where the rate of strain tensor is given by

$$\tau_{ij} = \frac{\partial u_i}{\partial x_j} + \frac{\partial u_j}{\partial x_i} - \frac{2}{3}\delta_{ij} \nabla \cdot \mathbf{u}. \tag{2.2}$$

Here, the rate of strain tensor corresponds to the ij^{th} component of the viscous stress. The body forces associated with the fluid are gravity and the Lorentz force which occurs under the presence of a magnetic field. The Lorentz force is given by

$$\mathbf{F}_L = \mathbf{j} \times \mathbf{B},$$

where $\mathbf{B}(\mathbf{x}, t)$ is the magnetic field, and

$$\mathbf{j} = \frac{1}{\mu_0} \nabla \times \mathbf{B},$$

where $\mathbf{j}(\mathbf{x}, t)$ is the current density. This is Ampère's law. Therefore, taking these forces into consideration we can express the momentum equation as

$$\rho \frac{\partial \mathbf{u}}{\partial t} + \rho(\mathbf{u} \cdot \nabla)\mathbf{u} = -\nabla P + \rho g \hat{\mathbf{z}} + \mathbf{j} \times \mathbf{B} + \mu \nabla \cdot (\tau). \tag{2.3}$$

We can express $\mu \nabla \cdot \tau$ as

$$\begin{aligned}
[\mu \nabla \cdot \tau]_i &= \mu \frac{\partial}{\partial xj}(\tau_{ij}) \\
&= \mu \frac{\partial}{\partial x_j} \left(\frac{\partial u_i}{\partial x_j} + \frac{\partial u_j}{\partial x_i} - \frac{2}{3}\delta_{ij} \nabla \cdot \mathbf{u} \right) \\
&= \mu \left(\frac{\partial^2 u_i}{\partial x_j \partial x_j} + \frac{\partial}{\partial x_i}[\nabla \cdot \mathbf{u}] - \frac{2}{3}\frac{\partial}{\partial x_i}[\nabla \cdot \mathbf{u}] \right) \\
&= \mu \left(\frac{\partial^2 u_i}{\partial x_j \partial x_j} + \frac{1}{3}\frac{\partial}{\partial x_i}[\nabla \cdot \mathbf{u}] \right) \\
&= \mu \left[\nabla^2 \mathbf{u} + \frac{1}{3} \nabla (\nabla \cdot \mathbf{u}) \right].
\end{aligned}$$

Equation (2.3) is described by four terms: $\rho(\mathbf{u}\cdot\nabla)\mathbf{u}$, which is responsible for the transfer of kinetic energy in the turbulent flow; ∇P, which is the pressure gradient; $\rho g\hat{\mathbf{z}}$, describes the gravity in the z-direction and, $\mu\nabla\cdot\tau$, is the shear stress.

We can represent the governing equation for the magnetic field using the induction equation:

$$\frac{\partial \mathbf{B}}{\partial t} = \nabla\times[\mathbf{u}\times\mathbf{B} - \eta\nabla\times\mathbf{B}]. \tag{2.4}$$

This must remain solenoidal at all times, that is, $\nabla\cdot\mathbf{B} = 0$. The induction equation implies that any initial solenoidal field should remain for all t. However, this is not always the case numerically. Because η is constant we can rewrite the second term in the induction equation using vector identities:

$$\nabla\times(\eta\nabla\times\mathbf{B}) = \eta\left(\cancelto{0}{\nabla(\nabla\cdot\mathbf{B})} - \nabla^2\mathbf{B}\right) = -\eta\nabla^2\mathbf{B}.$$

Hence,

$$\frac{\partial \mathbf{B}}{\partial t} = \nabla\times[\mathbf{u}\times\mathbf{B}] + \eta\nabla^2\mathbf{B}. \tag{2.5}$$

The first term in (2.5) represents induction due to fluid motions and the second term represents magnetic dissipation. It is important to rewrite (2.4) as (2.5) as it is more stable numerically.

The last equation determines the time evolution for the temperature, $T(\mathbf{x},t)$. This couples to the other governing equations via the pressure, which satisfies the equation of state for a perfect gas;

$$P = R_*\rho T.$$

Hence, T can be written as

$$\rho c_v\frac{\partial T}{\partial t} + \rho c_v(\mathbf{u}\cdot\nabla)T = -P\nabla\cdot\mathbf{u} + \nabla\cdot(K\nabla T) + \eta\mu_0|\mathbf{j}|^2 + \mu\frac{\tau^2}{2}. \tag{2.6}$$

Here, $\rho c_v(\mathbf{u}\cdot\nabla)T$ describes the advection of heat in the system, that is, the heat that is transferred by the flow of the fluid. Likewise, the other terms include $P\nabla\cdot\mathbf{u}$, which defines the heating that is contributed by pressure, $\nabla\cdot(K\nabla T)$ which is the heat flux and, lastly, $\mu\tau^2/2$ which is the amount of heat added to the system via viscous friction.

2.2.1 Non-dimensionalising the governing equations

We are now in a position to non-dimensionalise the governing equations. The scalings that have been used are

$$\begin{aligned}&\mathbf{x}\to\mathbf{x}'; \qquad t\to\frac{1}{\sqrt{R_*T_0}}t'; \qquad \mathbf{B}\to\sqrt{\mu_0\rho_0R_*T_0}\mathbf{B}';\\ &\mathbf{u}\to\sqrt{R_*T_0}\mathbf{u}'; \rho\to\rho_0\rho'; \qquad T\to T_0T'; \qquad P\to R_*\rho_0T_0P'.\end{aligned} \tag{2.7}$$

All the lengths have been scaled by 1 meaning that the domain has unit depth for this dimensionless system. Additionally, it is sensible to introduce some non-dimensional

parameters to simplify the final governing equations further. First, a dimensionless measure of stratification is given by $\theta = \Delta T/T_0$. Secondly, the polytropic index is $m = (g/R_*\Delta T) - 1$. Thermal diffusivity is defined as $\kappa = K/(\rho_0 c_p\sqrt{R_*T_0})$, and the Prandtl number is $\sigma = \mu c_p/K$. Lastly, we define $\zeta_0 = \eta c_P \rho_0/K$. These dimensionless parameters are discussed in detail in section 2.3.

Let us start with the equation for density as described in (2.1). Applying the scalings in (2.7) gives

$$\rho_0\sqrt{R_*T_0}\frac{\partial \rho'}{\partial t'} + \rho_0\sqrt{R_*T_0}(\mathbf{u}'\cdot\nabla')\rho' + \rho_0\sqrt{R_*T_0}\rho'\nabla'\cdot\mathbf{u}' = 0,$$

and with a simple division we obtain the dimensionless equation for the density:

$$\frac{\partial \rho'}{\partial t'} = -(\mathbf{u}'\cdot\nabla')\rho' - \rho'\nabla'\cdot\mathbf{u}'.$$

By applying the above scalings to the momentum equation we get

$$\begin{aligned}\rho_0 R_* T_0\rho'\frac{\partial \mathbf{u}'}{\partial t'} =& -\rho_0 R_* T_0\rho'(\mathbf{u}'\cdot\nabla')\mathbf{u}' - \rho_0 R_* T_0\nabla' P' \\ &+ \rho_0 g\rho'\hat{\mathbf{z}} + \frac{\mu_0\rho_0 R_* T_0}{\mu_0}(\nabla'\times\mathbf{B}')\times\mathbf{B}' + \mu\sqrt{R_*T_0}\nabla'\cdot\tau'.\end{aligned}$$

Dividing through by $\rho_0 R_* T_0$ leaves;

$$\begin{aligned}\rho'\frac{\partial \mathbf{u}'}{\partial t'} =& -\rho'(\mathbf{u}'\cdot\nabla')\mathbf{u}' - \nabla' P' + \frac{\Delta T}{T_0}\left(\frac{g}{R_*\Delta T} - 1 + 1\right)\rho'\hat{\mathbf{z}} \\ &+ (\nabla'\times\mathbf{B}')\times\mathbf{B}' + \frac{\mu c_p}{K}\frac{K}{c_p\rho_0\sqrt{R_*T_0}}\nabla'\cdot\tau'.\end{aligned}$$

This can be rewritten using the various dimensionless parameters:

$$\begin{aligned}\rho'\frac{\partial \mathbf{u}'}{\partial t'} =& -\rho'(\mathbf{u}'\cdot\nabla')\mathbf{u}' - \nabla' P' + \frac{\Delta T}{T_0}\left(\frac{g}{R_*\Delta T} - 1 + 1\right)\rho'\hat{\mathbf{z}} \\ &+ (\nabla'\times\mathbf{B}')\times\mathbf{B}' + \frac{\mu c_p}{K}\frac{K}{c_p\rho_0\sqrt{R_*T_0}}\nabla'\cdot\tau'.\end{aligned}$$

Hence, by using the above dimensionless parameters the dimensionless governing equation for momentum becomes

$$\frac{\partial \mathbf{u}'}{\partial t'} = -(\mathbf{u}'\cdot\nabla')\mathbf{u}' - \frac{1}{\rho'}\nabla' P' + \theta(m+1)\hat{\mathbf{z}} + \frac{1}{\rho'}(\nabla'\times\mathbf{B}')\times\mathbf{B}' + \frac{\sigma\kappa}{\rho'}\nabla'\cdot\tau'.$$

Next, we apply the scalings to the induction equation in (2.5):

$$B_0\sqrt{R_*T_0}\frac{\partial \mathbf{B}'}{\partial t'} = B_0\sqrt{R_*T0}\nabla'\times(\mathbf{u}'\times\mathbf{B}') - \eta\sqrt{\mu_0\rho_0 R_*T_0}\nabla'\times(\nabla'\times\mathbf{B}').$$

Dividing through and applying the dimensionless parameters to the above equation we get

$$\frac{\partial \mathbf{B}'}{\partial t'} = \nabla'\times(\mathbf{u}'\times\mathbf{B}') - \zeta_0\kappa\nabla\times(\nabla\times\mathbf{B}').$$

The equation of state becomes

$$R_*\rho_0 T_0 P' = R_*\rho_0\rho' T_0 T',$$

and dropping the primes shows

$$P = \rho T.$$

Lastly, the equation for heat becomes

$$\begin{aligned}\sqrt{R_*T_0}\rho_0 T_0 c_v\rho'\frac{\partial T'}{\partial t'} =& -\sqrt{R_*T_0}\rho_0 T_0 c_v\rho'(\mathbf{u}'\cdot\nabla')T' - \sqrt{R_*T_0}R_*\rho_0 T_0 P'\nabla'\cdot\mathbf{u}'\\ &+ T_0 K\nabla'^2 T' + \eta\rho_0 R_* T_0|\nabla'\times\mathbf{B}'|^2 + \mu R_* T_0\frac{\tau'^2}{2}.\end{aligned}$$

Tidying this up shows

$$\begin{aligned}\rho'\frac{\partial T'}{\partial t'} =& -\rho(\mathbf{u}'\cdot\nabla')T' - \frac{R_*P'}{c_v}\nabla'\cdot\mathbf{u}' + \frac{K}{\sqrt{R_*T_0}\rho_0 c_v}\nabla'^2 T'\\ &+ \frac{\eta R_*}{c_v\sqrt{R_*T_0}}|\nabla'\times\mathbf{B}'|^2 + \frac{\mu R_*}{\sqrt{R_*T_0}\rho_0 c_v}\frac{\tau'^2}{2}.\end{aligned}$$

Using the fact that $R_* = c_p - c_v = (\gamma-1)c_v$, we can reduce the above equation to

$$\begin{aligned}\rho'\frac{\partial T'}{\partial t'} =& -\rho'(\mathbf{u}'\cdot\nabla')T' - (\gamma-1)P'\nabla'\cdot\mathbf{u}' + \frac{K}{\rho_0 c_p\sqrt{R_*T_0}}\frac{c_p}{c_v}\nabla'^2 T'\\ &+ \frac{R_*}{c_v}\frac{\eta}{\sqrt{R_*T_0}}|\nabla'\times\mathbf{B}'|^2 + (\gamma-1)\frac{\mu c_p}{K}\frac{K}{\rho_0 c_p\sqrt{R_*T_0}}\frac{\tau'^2}{2}.\end{aligned}$$

Again, the use of the dimensionless parameters defined above shows that

$$\frac{\partial T'}{\partial t'} = -(\mathbf{u}'\cdot\nabla')T' - \frac{(\gamma-1)P'}{\rho'}\nabla'\cdot\mathbf{u}' + \frac{\kappa\gamma}{\rho'}\nabla'^2 T' + \frac{(\gamma-1)\zeta_0\kappa}{\rho'}|\nabla'\times\mathbf{B}'|^2 + \frac{(\gamma-1)\sigma\kappa}{\rho'}\frac{\tau'^2}{2}.$$

Therefore, with these deductions, we can drop the primes and hence the governing equations for the density $\rho(\mathbf{x},t)$, fluid velocity $\mathbf{u}(\mathbf{x},t)$, induction equation $\mathbf{B}(\mathbf{x},t)$ and temperature $T(\mathbf{x},t)$ in a dimensionless form are:

$$\frac{\partial\rho}{\partial t} = -(\mathbf{u}\cdot\nabla)\rho - \rho\nabla\cdot\mathbf{u}, \tag{2.8}$$

$$\frac{\partial\mathbf{u}}{\partial t} = -(\mathbf{u}\cdot\nabla\mathbf{u}) - \frac{1}{\rho}\nabla P + \theta(m+1)\hat{\mathbf{z}} + \frac{1}{\rho}(\nabla\times\mathbf{B})\times\mathbf{B} + \frac{\kappa\sigma}{\rho}\nabla\cdot\tau, \tag{2.9}$$

$$\frac{\partial\mathbf{B}}{\partial t} = \nabla\times(\mathbf{u}\times\mathbf{B}) - \zeta_0\kappa\nabla\times(\nabla\times\mathbf{B}), \tag{2.10}$$

$$\begin{aligned}\frac{\partial T}{\partial t} =& -(\mathbf{u}\cdot\nabla)T - (\gamma-1)T\nabla\cdot\mathbf{u} + \frac{\kappa\gamma}{\rho}\nabla^2 T\\ &+ \frac{\kappa(\gamma-1)}{\rho}\left(\sigma\frac{|\tau|^2}{2} + F\zeta_0|\nabla\times\mathbf{B}|^2\right).\end{aligned} \tag{2.11}$$

Finally, boundary conditions are now set at $z = 0$ and $z = 1$. In dimensionless units, the fixed temperatures correspond to $T = 1$ at $z = 0$ and $T = 1 + \theta$ at $z = 1$. Here, $\theta = 3$ meaning that the temperature differs by a factor of four within the box. The magnetic field boundary conditions at $z = 0$ and $z = 1$ correspond to a vertical field ($B_x = B_y = \partial B_z/\partial z = 0$). The magnetic field is initialised from a small seed field with zero net flux. In a hydrostatic case, a solution to the governing equations is given by the equilibrium solution:

$$T = 1 + \theta z; \;\; \rho = (1 + \theta z)^m; \;\; \mathbf{u} = \mathbf{0}, \tag{2.12}$$

which corresponds to a hydrostatic polytropic layer (see Matthews et al. 1995). The values of m and θ are fixed as 1 and 3 respectively, as this ensures the solution is far away from the convective stability boundary.

2.3 Model parameters

The evolution of the system is determined by various dimensionless parameters which, as in Bushby & Favier (2011), are defined in Table 1. The first parameter γ, is the ratio of specific heat capacities. For an ideal gas, $\gamma = 1 + 2/f$, where f is the number of dimensions in phase space. Hence, as $f = 3$ a choice of $\gamma = 5/3$ is appropriate for a monatomic gas. Next, the polytropic index is defined to be $m = 1$ as this implies convective instability within the fluid. The thermal stratification is $\theta = 3$. The Prandtl number is the ratio of momentum diffusivity to thermal diffusivity. Within the solar convection zone $\sigma \ll 1$, suggesting that the system is dominated by thermal diffusivity. However, as the model is simplistic and computational constraints restrict us, a value of $\sigma = 1$ is chosen for numerical convenience. An appropriate value for the thermal diffusivity is $\kappa = 0.00548$.

Table 1: Non-dimensional parameters in the model (Bushby & Favier 2011, p.4).

Parameter	Definition	Description	Value
γ	c_p/c_v	Ratio of specific heat capacities	5/3
m	$(g/R_*\Delta T) - 1$	Polytropic index	1.0
θ	$\Delta T/T_0$	Thermal stratification	3.0
σ	$\mu c_p/K$	Prandtl number	1.0
κ	$K/\rho_0 c_p (R_* T_0)^{1/2}$	Dimensionless thermal diffusivity	0.00548
ζ_0	$\eta\rho_0 c_p/K$	Ratio of magnetic to thermal diffusivities	0.32

There are four important parameters focussed on in this model: one of them is the mid-layer Rayleigh number, which is a dimensionless measure of how heat is transferred in the fluid. If the Rayleigh number is below a critical value of ≈ 900 we see that heat transfer is mainly in the form of conduction. If this value is exceeded then the heat is transferred primarily via convection. This is important as we want the fluid to be convective; that is, we want the Rayleigh number to be much larger than $Ra_{\rm crit}$. Therefore, the Rayleigh number is defined as

$$Ra = (m + 1 - m\gamma)(1 + \frac{\theta}{2})^{2m-1} \frac{(m + 1)\theta^2}{\kappa^2 \gamma \sigma}, \tag{2.13}$$

and with the above parameter choices, $Ra \approx 300000$ which ensures that the resulting convection is energetic and time-dependent. When working with fluid models, it is often worth observing the Reynolds number as it provides an idea of what measure of turbulence is present in the flow. I have chosen the same definition as in Bushby & Favier (2014):

$$Re = \frac{\rho_{mid} U_{rms}}{\kappa \sigma}, \tag{2.14}$$

where U_{rms} is the total root mean square velocity, and ρ_{mid} is the mean density at the mid-layer of the domain. The above parameters give a value of $Re \approx 153$. In the solar photosphere $Re \approx 10^{12}$, with higher values not possible for us due to computational constraints (Ossendrijver 2003). The magnetic Reynolds number is

$$Rm = \frac{U_{rms}}{\kappa \zeta_0}. \tag{2.15}$$

and with our parameter choices, $Rm \approx 205$. A value of $Rm \gg 1$ ensures that the flux lines of the magnetic field are advected with the fluid flow, as in the solar surface. However, our value of Rm is very small when compared to the Sun where $Rm \approx 10^6$ (Ossendrijver 2003). Lastly, the mid-layer magnetic prandtl number is

$$Pm = \frac{Rm}{Re}. \tag{2.16}$$

Within the Sun, $Pm \ll 1$, however in the simulation it has been set equal to 1 as lower values are inaccessible due to computational constraints.

3. Spectra

Turbulent convection in the solar convection zone is characterised by the superposition of a large number of scales within the turbulent spectrum. It is observing the physics of such a system that leads us to ask the question: If a scale such as mesogranulation is present, how would we identify and characterise it? For granulation, there is clearly a distinction from other scales due to the fact that granulation shows the highest contrast in intensity and the largest fluctuation of velocity. However, for mesogranulation it is not clear how to characterise such a scale. In Figure 2.2, at the lower depths, there is evidence that scales larger than that of granulation are present. Therefore, it is sensible to do a power spectrum analysis to see whether or not a scale exists in the kinetic energy spectrum that is as transparent, but larger than granulation. To calculate the kinetic energy spectra we start from the definition of kinetic energy:

$$\text{Kinetic energy} = \frac{1}{2}|\mathbf{U}|^2.$$

Integrating this over the volume V of the box gives

$$\frac{1}{2}\int_V (u^2+v^2+w^2)\,\mathrm{d}x\,\mathrm{d}y\,\mathrm{d}z = \frac{1}{2}\int_V |f|^2\,\mathrm{d}x\,\mathrm{d}y\,\mathrm{d}z. \tag{3.1}$$

Here, the first integral has been rewritten as a real general periodic function, f. The discrete Fourier transform of f can be written as

$$f(x,y,z,t) = \sum_{l=0}^{N-1}\sum_{m=0}^{N-1} \hat{f}_{lm}(z,t)\exp\left(\frac{-2\pi i l x}{\lambda}\right)\exp\left(\frac{-2\pi i m y}{\lambda}\right). \tag{3.2}$$

The complex conjugate of this is

$$f^*(x,y,z,t) = \sum_{l'=0}^{N-1}\sum_{m'=0}^{N-1} \hat{f}^*_{l'm'}(z,t)\exp\left(\frac{2\pi i l' x}{\lambda}\right)\exp\left(\frac{2\pi i m' y}{\lambda}\right). \tag{3.3}$$

Hence, using the fact that $|f|^2 = ff^*$ we can substitute (3.2) and (3.3) into (3.1):

$$\begin{aligned}
\frac{1}{2}\int_0^1\int_0^\lambda\int_0^\lambda |f^2|\,\mathrm{d}x\,\mathrm{d}y\,\mathrm{d}z &= \frac{1}{2}\int_0^1\int_0^\lambda\int_0^\lambda \left[\sum_{l=0}^{N-1}\sum_{m=0}^{N-1}\hat{f}_{lm}(z,t)\exp\left(\frac{-2\pi i l x}{\lambda}\right)\exp\left(\frac{-2\pi i m y}{\lambda}\right)\right] \\
&\quad\times\left[\sum_{l'=0}^{N-1}\sum_{m'=0}^{N-1}\hat{f}^*_{l'm'}(z,t)\exp\left(\frac{2\pi i l' x}{\lambda}\right)\exp\left(\frac{2\pi i m' y}{\lambda}\right)\right]\mathrm{d}x\,\mathrm{d}y\,\mathrm{d}z \\
&= \frac{1}{2}\int_0^1\int_0^\lambda\int_0^\lambda \sum_{l=0}^{N-1}\sum_{m=0}^{N-1}\sum_{l'=0}^{N-1}\sum_{m'=0}^{N-1}\hat{f}_{lm}(z,t)\hat{f}^*_{l'm'}(z,t) \\
&\quad\times\exp\left(\frac{-2\pi i(l-l')x}{\lambda}\right)\exp\left(\frac{-2\pi i(m-m')y}{\lambda}\right)\mathrm{d}x\,\mathrm{d}y\,\mathrm{d}z.
\end{aligned}$$

Next, we can rewrite this integral in terms of cosine and sine:

$$\begin{aligned}\int_0^1\int_0^\lambda\int_0^\lambda |f^2|\,\mathrm{d}x\,\mathrm{d}y\,\mathrm{d}z = \frac{1}{2}\int_0^1\int_0^\lambda\int_0^\lambda \sum_{l=0}^{N-1}\sum_{m=0}^{N-1}\sum_{l'=0}^{N-1}\sum_{m'=0}^{N-1} \hat{f}_{lm}(z,t)\hat{f}^*_{l'm'}(z,t) \\ \times\left[\cos\left(\frac{-2\pi(l-l')x}{\lambda}\right) - i\sin\left(\frac{-2\pi(l-l')x}{\lambda}\right)\right] \\ \times\left[\cos\left(\frac{-2\pi(m-m')y}{\lambda}\right) - i\sin\left(\frac{-2\pi(m-m')y}{\lambda}\right)\right]\mathrm{d}x\,\mathrm{d}y\,\mathrm{d}z.\end{aligned}$$

Let us now examine the integrals over x and y. For these two integrals there are four posibilities to consider:

1. $l \neq l' \quad \& \quad m \neq m'$;
2. $l \neq l' \quad \& \quad m = m'$;
3. $l = l' \quad \& \quad m \neq m'$;
4. $l = l' \quad \& \quad m = m'$.

Starting with case 2., let us observe what happens to the above integral:

$$\begin{aligned}\int_0^\lambda\int_0^\lambda |f^2|\,\mathrm{d}x\,\mathrm{d}y &= \int_0^\lambda\int_0^\lambda \left[\cos\left(\frac{-2\pi(l-l')x}{\lambda}\right) - i\sin\left(\frac{-2\pi(l-l')x}{\lambda}\right)\right] \\ &\quad\times\left[\cos(0) - i\sin(0)\right]\mathrm{d}x\,\mathrm{d}y \\ &= \int_0^\lambda \left[\cos\left(\frac{-2\pi(l-l')x}{\lambda}\right) - i\sin\left(\frac{-2\pi(l-l')x}{\lambda}\right)\right][x]_0^\lambda\,\mathrm{d}y \\ &= \int_0^\lambda \lambda\left[\cos\left(\frac{-2\pi(l-l')x}{\lambda}\right) - i\sin\left(\frac{-2\pi(l-l')x}{\lambda}\right)\right]\mathrm{d}y \\ &= \int_0^\lambda \frac{\lambda^2}{2\pi(l-l')}\left[\sin\left(\frac{2\pi(l-l')x}{\lambda}\right) + i\cos\left(\frac{2\pi(l-l')x}{\lambda}\right)\right]_0^\lambda\mathrm{d}y \\ &= \int_0^\lambda \frac{\lambda^2}{2\pi(l-l')}\left[\left(\cancelto{0}{\sin(-2\pi(l-l'))} + i\cancelto{1}{\cos(2\pi(l-l'))}\right)\right] \\ &\quad - \frac{\lambda^2}{2\pi(l-l')}\left[(\sin(0) + i\cos(0))\right] \\ &= \int_0^\lambda 0\,\mathrm{d}y = 0.\end{aligned}$$

Clearly, whenever $l \neq l'$ the integral will be zero. Therefore, to avoid a null case we set $l = l'$, leaving only cases 3. and 4. as possible options. Hence, let us now observe what happens to the x and y integrals for the case where $l = l'$ and $m \neq m'$:

$$\begin{aligned}
\int_0^\lambda \int_0^\lambda |f^2| \,\mathrm{d}x\,\mathrm{d}y &= \int_0^\lambda \int_0^\lambda [\cos(0) - i\sin(0)] \\
&\quad \times \left[\cos\left(\frac{-2\pi(m-m')y}{\lambda}\right) - i\sin\left(\frac{-2\pi(m-m')y}{\lambda}\right)\right] \mathrm{d}x\,\mathrm{d}y \\
&= \int_0^\lambda \left[\cos\left(\frac{2\pi(m-m')y}{\lambda}\right) - i\sin\left(\frac{2\pi(m-m')y}{\lambda}\right)\right] [x]_0^\lambda \,\mathrm{d}y \\
&= \int_0^\lambda \lambda \left[\cos\left(\frac{2\pi(m-m')y}{\lambda}\right) - i\sin\left(\frac{2\pi(m-m')y}{\lambda}\right)\right] \mathrm{d}y \\
&= \frac{\lambda^2}{2\pi(m-m')} \left[\sin\left(\frac{2\pi(m-m')y}{\lambda}\right) + i\cos\left(\frac{2\pi(m-m')y}{\lambda}\right)\right]_0^\lambda \\
&= \left[\left(\cancelto{0}{\sin(-2\pi(m-m'))} + i\cancelto{1}{\cos(2\pi(m-m'))}\right)\right] \\
&\quad - [(\sin(0) + i\cos(0))] \\
&= \int_0^\lambda 0 \,\mathrm{d}y = 0.
\end{aligned}$$

Again we get a null case. Thus, we must have $l = l'$ and $m = m'$ as the only possibility. So, the integrals over x and y must reduce to

$$\begin{aligned}
\int_0^\lambda \int_0^\lambda |f^2| \,\mathrm{d}x\,\mathrm{d}y &= \int_0^\lambda \int_0^\lambda [\cos(0) - i\sin(0)] \times [\cos(0) - i\sin(0)] \,\mathrm{d}x\,\mathrm{d}y \\
&= \int_0^\lambda \int_0^\lambda 1 \,\mathrm{d}x\,\mathrm{d}y = \int_0^\lambda \lambda \,\mathrm{d}y = \lambda^2.
\end{aligned}$$

Now, we are now left with a much simpler integral that only involves integration over z;

$$\int_0^1 \int_0^\lambda \int_0^\lambda |f^2| \,\mathrm{d}x\,\mathrm{d}y\,\mathrm{d}z = \frac{\lambda^2}{2} \int_0^1 \sum_{l=0}^{N-1} \sum_{m=0}^{N-1} |\hat{f}_{lm}(z,t)|^2 \,\mathrm{d}z. \tag{3.4}$$

To work with this integral let us define

$$I = \sum_{l=0}^{N-1} \sum_{m=0}^{N-1} |\hat{f}_{lm}(z,t)|^2$$

and make an approximation over the continuum for I:

$$I \approx \int_0^\infty \int_0^\infty |\hat{f}(k_x, k_y)|^2 \,\mathrm{d}k_x\,\mathrm{d}k_y.$$

We further assume that there is no preferred direction, i.e. horizontal isotropy. Therefore, we can integrate with respect to $\mathrm{d}k_x$, $\mathrm{d}k_y$, where k_x, k_y are the components of the wave vector. We make the integration easier by changing into polar coordinates:

$$I \approx \int_0^{2\pi} \int_0^\infty |\hat{f}(k,z)|^2 k \,\mathrm{d}k\,\mathrm{d}\varphi = 2\pi \int_0^\infty |\hat{f}(k,z)|^2 k \,\mathrm{d}k$$

Here, $\mathrm{d}k$ is the integral over the wavenumbers, $\mathrm{d}\varphi$ is the integral over the wavenumber angle and k is the Jacobian determinant. Now, we can plug this back into (3.4) giving

$$\begin{aligned}\int_0^1\int_0^\lambda\int_0^\lambda |f^2|\,\mathrm{d}x\,\mathrm{d}y\,\mathrm{d}z &= \int_0^1\int_0^\infty \lambda^2 k\pi|\hat{f}(k,z)|^2\,\mathrm{d}k\,\mathrm{d}z\\ &= \int_0^\infty\int_0^1 \lambda^2 k\pi|\hat{f}(k,z)|^2\,\mathrm{d}z\,\mathrm{d}k.\end{aligned}$$

The order of integration does not matter here. Therefore, this is a representation of the kinetic energy spectrum in the form of an integral:

$$\int_0^\infty E(k)\,\mathrm{d}k,$$

where the kinetic energy spectrum is defined as

$$E(k) = \int_0^1 \lambda^2 k\pi|\hat{f}(k,z)|^2\,\mathrm{d}z. \tag{3.5}$$

The plot of the time averaged kinetic energy spectrum against all wave numbers for "a range of layers in the box" is shown in Figure 3.1. The peak in both graphs at low wave numbers shows me that mesogranulation is clearly present at all depths, for both data sets. However, the peak is at different wave numbers for each graph. That is, for data set 1, $k \approx 6$, whereas, $k \approx 3$ for data set 2. This discrepancy is due to the different box sizes used in the data sets. Visually, the mesogranular peak equates to the horizontal scales that are illustrated at depths $z = 0.4, 0.6$ in Figure 2.2.

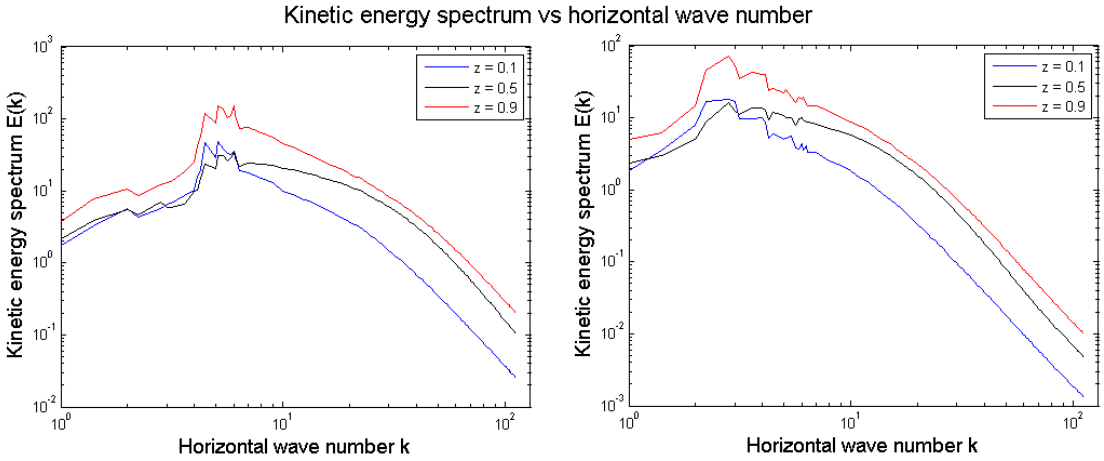

Figure 3.1: A plot of the kinetic energy spectrum for both data sets against all horizontal wave numbers for depths, $z = 0.1, 0.5, 0.9$. The graph on the left shows data set 1 with $\lambda = 20$. Similarly, the graph on the right is data set 2 where $\lambda = 10$.

It is clear that mesogranulation is a strong feature of this system. This shows that it is possible to find mesogranulation in both a relatively small $10 \times 10 \times 1$ domain

and larger. Additionally, the above graphs are similar to those in previous studies of both Boussinesq and compressible convection, providing further validity to my results (Bushby & Favier 2014; Busby & Favier 2011; Cattaneo et al. 2001).

In the next chapter, I will implement tracking algorithms on the simulation to see whether they can re-produce the above kinetic energy spectrum and hence, show the reliability of correlation tracking algorithms.

4. Tracking algorithms

Correlation tracking algorithms are one of the most common methods used to determine solar surface velocity fields. They involve observing various structures visible at the surface of the Sun over a period of time. There are three main algorithms used by researchers today, all applying similar techniques:

1. Local correlation tracking (LCT),
2. Coherent structure tracking (CST),
3. Ball tracking (BT).

The first algorithm, local correlation tracking works by maximising the correlation between small sub-images to determine the motion of features on consecutive snapshots at a certain time. Coherent structure tracking, determines coherent structures between images and measures their displacement over time. Lastly, ball tracking works by adding balls to the flow and tracking their movement as the flow develops in time.

Local correlation tracking considers every pixel in both images, which contrasts with coherent structure tracking as it segments the image and considers where these larger segments move. Due to the fact that LCT considers each pixel it is my belief that it is more reliable, and for that reason I will implement an LCT algorithm on the simulation. Although, it is my belief that LCT is the most reliable algorithm, it should be noted that none of these algorithms are perfect and the techniques themselves, incorporate no physical conservation laws. Therefore, because of these imperfections I will take care when interpreting the results from the LCT routine.

4.1 Fourier local correlation tracking

The fathers of local correlation tracking are considered to be November & Simon (1988) whose method shifts images at nine integer-pixel spatial lags then computes a cross-correlation for each shift. The many LCT routines used by researchers today all work by using one principal idea. Proper motion or displacement between separate images is found by maximising a cross-correlation function. For my dissertation I will use a Fourier local correlation tracking algorithm (FLCT) from Welsch (2004), adapting their routine to work in Matlab.

The algorithm involves six major steps:

1. Selecting the image,
2. Multiplying each image by a Gaussian window function,
3. Creating the reduced size images,
4. Computing the cross-correlation function,

5. Locating the displacement that maximises the cross-correlation function,
6. Calculating the velocities: $v_x(i,j) = \delta x * \delta s/\delta t$ and $v_y(i,j) = \delta y * \delta s/\delta t$.

Now, let us describe the algorithm in detail:

4.1.1 Selecting the image

The idea behind the FLCT algorithm is that given two, 2-dimensional images $I_1(x, y, t_1)$ and $I_2(x, y, t_2)$, with the second image taken slightly after the first one, so that $t_2 = t_1 + \delta t$, we can calculate the 2-dimensional flow field: $v_x(x, y)$, $v_y(x, y)$. Then, when we apply the flow $v_x(x, y)$, $v_y(x, y)$ to the scalar field in the first image, it should resemble the second image.

To construct the 2-dimensional velocity field, we must begin at a certain location within both images. In FLCT, we calculate the maximum between both images and compute the velocity vectors for all the points that are within a certain threshold. Threshold is a free parameter in FLCT and the optimal value is discussed in chapter 5.

4.1.2 The Gaussian window function

For the pixels at which we wish to compute a velocity vector, we multiply by a windowing function to de-emphasise the parts of the image away from the pixel. FLCT does this by multiplying each of the images to be considered by a Gaussian window function of width α, which is centered at the location of the maximum, (x_i, y_j). This is defined as

$$S_{1(i,j)}(x, y) = I_{1(i,j)}(x, y) \exp(-\left[(x - x_i)^2 + (y - y_i)^2\right]/\alpha^2),$$
$$S_{2(i,j)}(x, y) = I_{2(i,j)}(x, y) \exp(-\left[(x - x_i)^2 + (y - y_i)^2\right]/\alpha^2),$$

where $S_{1(i,j)}(x, y)$ and $S_{2(i,j)}(x, y)$ represent 'sub-images'. A 2-dimensional Gaussian function has been chosen because it is a well known distribution that appears repeatedly in real life observations. In particular, the Gaussian distribution is a pragmatic choice for our data as it will maximise the entropy for the given energy whilst smoothing the data so as to only focus on the important areas. Moreover, different window functions were evaluated in Louis et al. (2015), who found that a Gaussian window was an efficient window choice. Figure 4.1 shows the Gaussian curve in a 3-dimensional domain. It is easy to see how the points away from the maximum are de-emphasised.

The window size, α, is an important parameter as it defines the size of the region of interest. That is, α encompasses the flow structure around the pixel we are considering. Like threshold, α is a free paramter in FLCT with optimal values discussed in chapter 5.

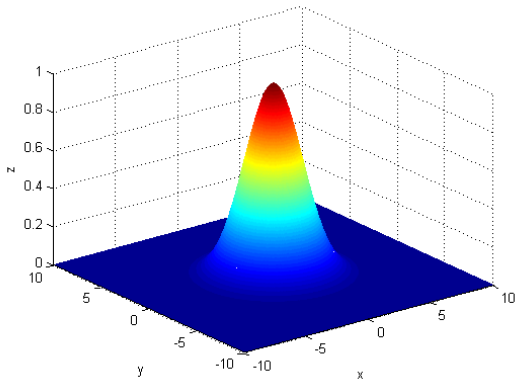

Figure 4.1: Gaussian function similar to that in the routine.

4.1.3 The reduced size images

The next step is to create reduced size images that surround the sub-images. This is done to stop MATLAB looping over the entire array for each pixel, considering many insignificant values. This process is shown pictorially in Figure 4.2, with three detailed steps to explain.

1. First, let us consider two sub-images, $S_{1(i,j)}(x, y)$ and $S_{2(i,j)}(x, y)$, separated in time by δt. In figure 4.2 the sub-images are represented by the ellipses, where everything inside is considered as significant. For both the images, the algorithm loops over all the values in x, from 1 to 512 stopping when we find a value of x that is within a certain tolerance of the of the sub-images. These values of x are defined as iminS1 and iminS2 for images S1 and S2, respectively. Then we repeat the same operation, but loop over the values of x from 512 to 1 in steps of -1 until again, we are within a certain tolerance of the sub-images. These values of x are defined as imaxS1 and imaxS2 for images S1 and S2, respectively. This operation is then repeated for the y direction in both images. The resulting values are labelled jminS1, jmaxS1, jminS2 and jmaxS2. These, four operations for both images create a box, centred at the maximum, which surround the sub-images.

2. The first step, above, only defines a box around the significant parts in the image it is considering. This leaves a problem. We need one box that encompasses the significant areas in both images. To solve this problem, we take the smallest 'minimum' from the x and y directions in both images to give a lower bound. Repeating this operation for the maximum values and taking the largest 'maximum' gives an upper bound in the x and y directions. These bounds form the 'reduced size image'.

3. An illustration of the resulting reduced size images is superimposed upon images I_1 and I_2.

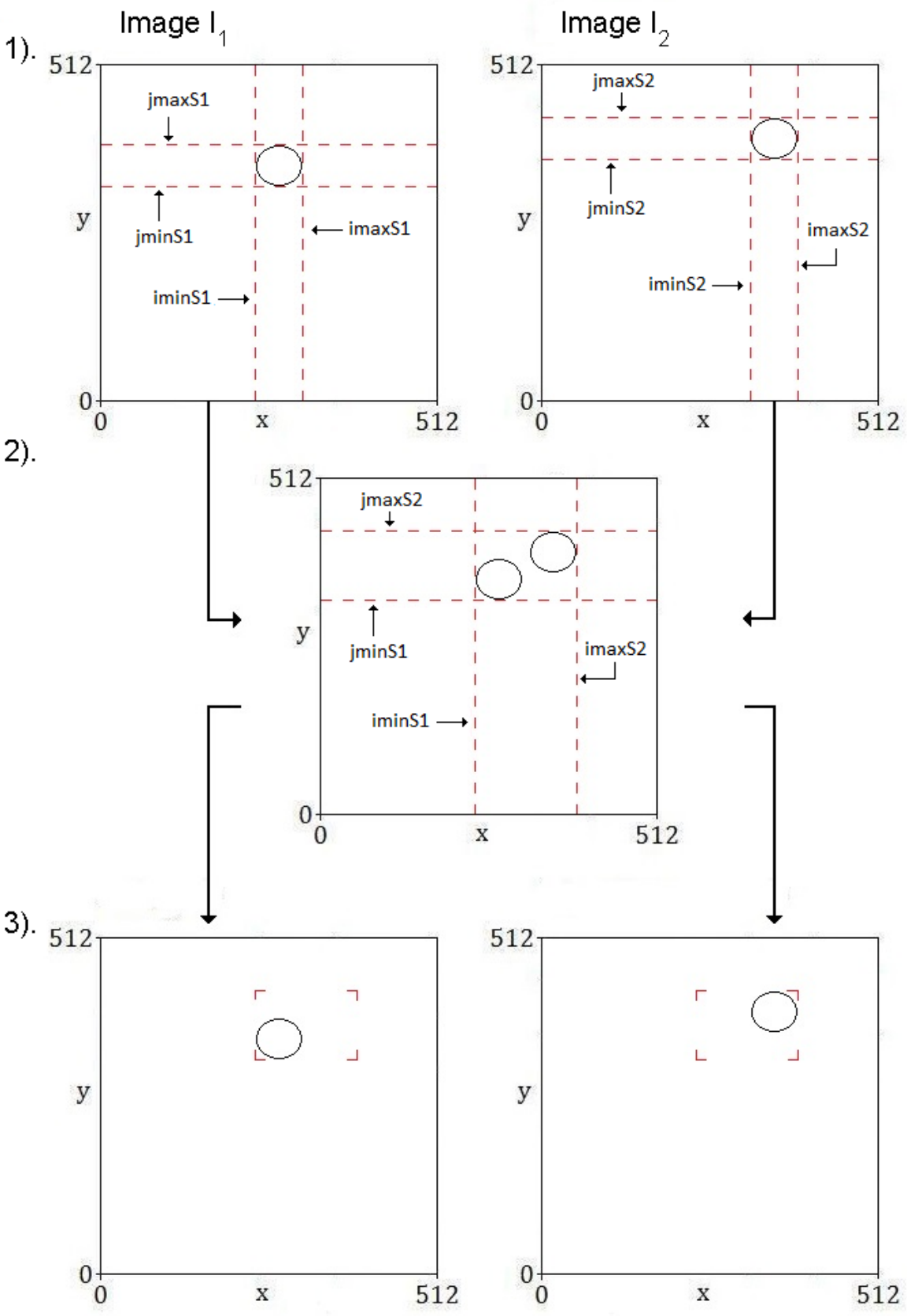

Figure 4.2: This figure shows how the computational routine crops the images to create one reduced size image that encompasses both the significant areas from image I_1 and image I_2.

4.1.4 Calculating the cross correlation function

We now calculate the cross correlation function between the two sub-images, $S_{1(i,j)}$ and $S_{2(i,j)}$. The cross-correlation function for the (i,j)th pixel is

$$\begin{aligned} C_{i,j}(\delta x, \delta y) &= S_{1(i,j)}(x,y) \star S_{2(i,j)}(x,y) \\ &= \int_{-\infty}^{\infty}\int_{-\infty}^{\infty} S^*_{1(i,j)}(-x,-y) S_{2(i,j)}(\delta x - x, \delta y - y)\,\mathrm{d}x\,\mathrm{d}y, \end{aligned} \tag{4.1}$$

where δx and δy represent the shifts in the x and y direction, respectively, between the two consecutive images. Here, $\star$ denotes the cross-correlation and $S^*_{1(i,j)}$ is the complex conjugate of $S_{1(i,j)}$. FLCT calculates $C(\delta x, \delta y)$ by using the convolution theorem to rewrite (4.1) in terms of Fourier transforms (Fisher 2008). Let us define the Fourier transforms of $S_{1(i,j)}(x,y)$ and $S_{2(i,j)}(x,y)$ as

$$\begin{aligned} S_1(x,y) &\equiv \mathcal{F}^{-1}_{i,j}\left[s(k_x,k_y)\right](x,y) = \int\int s(k_x,k_y)\exp(2\pi i(k_x x + k_y y))\,\mathrm{d}k_x\,\mathrm{d}k_y, \\ S_2(x,y) &\equiv \mathcal{F}^{-1}_{i,j}\left[s(k_x,k_y)\right](x,y) = \int\int s(k_x,k_y)\exp(2\pi i(k_x(\delta x + x) + k_y(\delta y + y)))\,\mathrm{d}k_x\,\mathrm{d}k_y. \end{aligned}$$

Then, using the convolution theorem shows

$$\begin{aligned} S_1 \star S_2 &= \int\int S_1^*(-x,-y) S_2(\delta x - x, \delta y - y)\,\mathrm{d}x\,\mathrm{d}y \\ &= \int\int S_1^* \left[\int\int \hat{s}_2 \exp(2\pi i(k_x(\delta x - x) + k_y(\delta y - y)))\,\mathrm{d}k_x\,\mathrm{d}k_y\right]\mathrm{d}x\,\mathrm{d}y \\ &= \int\int \hat{s}_2 \left[\int\int S_1^* \exp(-2\pi i(k_x x + k_y y))\,\mathrm{d}x\,\mathrm{d}y\right]\exp(2\pi i(k_x\delta x + k_y \delta y))\,\mathrm{d}k_x\,\mathrm{d}k_y \\ &= \int\int \hat{s}_2 \hat{s}_1^* \exp(2\pi i(k_x\delta x + k_y\delta y))\,\mathrm{d}k_x\,\mathrm{d}k_y \\ &\equiv \mathcal{F}^{-1}_{k_x,k_y}[\hat{s}_1^*\hat{s}_2](x,y). \end{aligned}$$

Here, $\mathcal{F}^{-1}_{k_x,k_y}[\hat{F}_1^*\hat{F}_2](x,y)$ is the inverse Fourier transform. Thus, the cross correlation is

$$C_{i,j}(\delta x, \delta y) = \mathcal{F}^{-1}_{k_x,k_y}[\hat{s}^*_{1(i,j)}(k_x,k_y)\hat{s}_{2(i,j)}(k_x,k_y)](x,y). \tag{4.2}$$

4.1.5 Determining the shifts

The cross correlation function is a measure of similarity between the two sub-images. It fixes the second image then shifts the first image across the second image until all possible positions have been covered. We want to find the shifts δx and δy that maximise the cross correlation function, as it is this point where the sub-images are most similar. That is, it is the point where we move sub-image 1 to get sub-image 2. This works due to the fact that when the peaks in $S_{1(i,j)}$ match the peaks in $S_{2(i,j)}$, we get a large contribution to $C_{i,j}(\delta x, \delta y)$. Similarly, when the troughs match, the two negative numbers give a positive number which also provides a large contribution to $C_{i,j}(\delta x, \delta y)$. In FLCT, the peak of $|C_{i,j}(\delta x, \delta y)|$ is calculated, so that we avoid complex arithmetic.

4.1.6 Calculating the velocities

The maximum of $|C_{i,j}(\delta x, \delta y)|$ gives us the shifts δx and δy. Then, multiplying by pixel size, δs and dividing by time separation, δt results in a velocity, and thus a velocity field can be created.

Quite often, higher order techniques such as interpolation are used to locate the maximum to 'sub-pixel' resolution (Welsch 2004; Welsch 2007). The reason for this is that the data gathered from solar observations is usually very noisy and low resolution, and higher order techniques achieve more accurate results. However, as my data has come from a simulation it is much more resolved than observational data meaning that it is more beneficial to save time computationally and accept the small error. This error will be only $+/-1$ pixel, which, in a large domain with well resolved data is irrelevant. Hence, I chose not to implement any higher order techniques.

4.2 Testing the code

To verify that the code was working correctly, I created a test code that employed my FLCT technique to two smaller images that I knew the results for. The functions I opted for were

$$I_1(x, y) = \sin\left(\frac{\pi x}{50}\right) \sin\left(\frac{\pi y}{50}\right),$$

$$I_2(x, y) = \sin\left(\frac{\pi(x-1)}{50}\right) \sin\left(\frac{\pi(y-3)}{50}\right),$$

which are defined over the domain $0 \leq x, y \leq 50$. The image I_2 is treated as the lagged image, where $I_2 = I_1 + \delta t$, and is a translation of $+1$ in the x direction, and $+3$ in the y direction. These are sensible choices as functions because they define a simple uniform shift. To illustrate this, the functions are plotted in Figure 4.3.

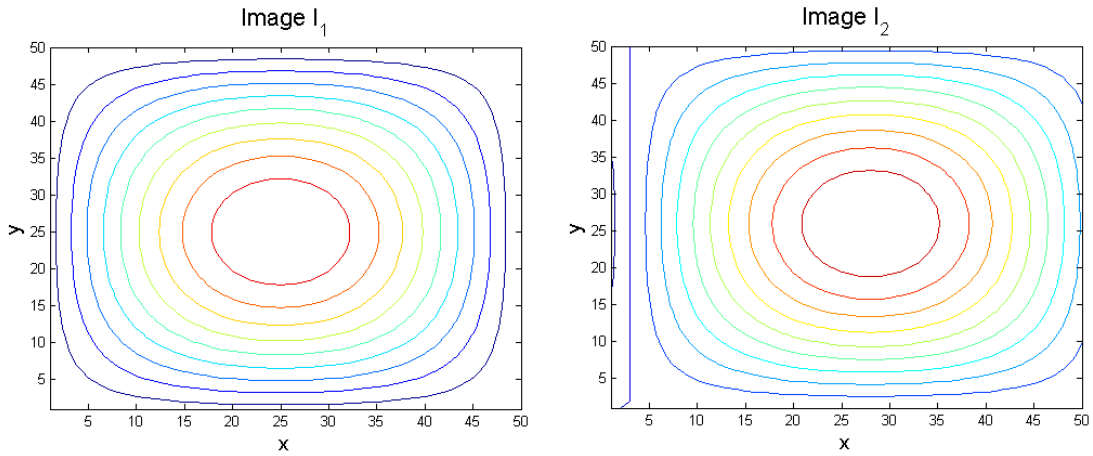

Figure 4.3: The two images I_1 and I_2 over the domain $0 \leq x, y \leq 50$.

As these functions are purely for test purposes, the domain has been shrunk massively as there is no point in wasting time computationally. Some parameters have

been changed to compensate this as their optimal values change due to different factors. Secondly, there is no time difference between the two functions, so δt has been left the same as in the simulation. This will not affect the final result.

The code gave me shifts of $\delta x = +1$ and $\delta y = +3$. I plotted the velocity field, shown in figure 4.4, to illustrate this. Furthermore, I checked negative shifts by interchanging the two images I_1 and I_2. Values of $\delta x = -1$ and $\delta y = -3$ were returned, verifying that the FLCT algorithm works for both positive and negative shifts. As a final sanity check I replaced $I_2(x, y)$ with $I_1(x, y)$ so that there was no difference between either image. The FLCT routine returned values of $\delta x = 0$ and $\delta y = 0$, as expected.

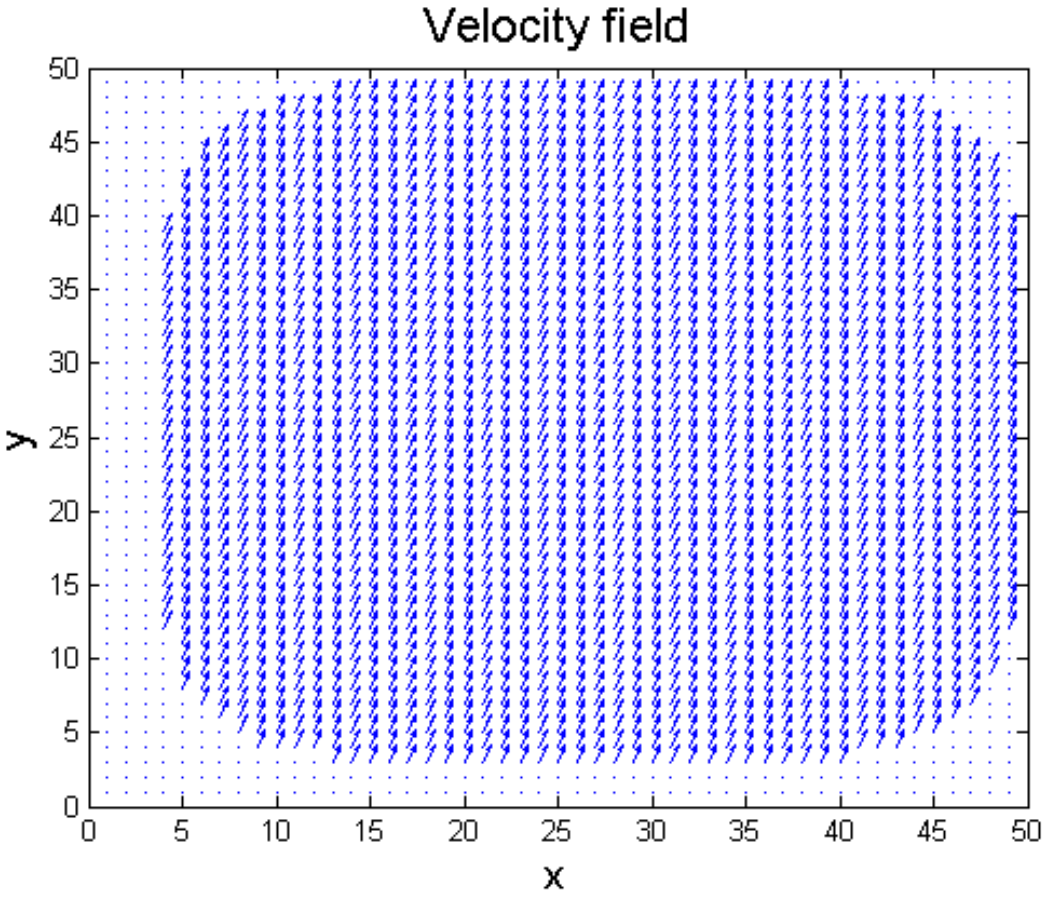

Figure 4.4: The resulting velocity field between images I_1 and I_2.

5. Application to simulation data

5.1 Testing

I found that when I used temperature maps as the FLCT input variable, no velocity field could be created. For the routine, we have considered the temperature maximum, which lies at the granules center. No velocity field is created due to the fact that the maxima in the images are too broad. That is, the areas we are considering are quite wide. A solution to this problem could be to consider the temperature minimum, which lies in the narrow intergranular lanes. This is clearly an area for future research. The problem with the temperature means that like researchers we have to use a proxy to calculate the velocity field. Hence, as the magnetic field distribution follows the flow accumulating preferentially at the boundaries of granules, I will use the magnetic field. It is noteworthy, that in the past, researchers have preferred intensity maps as their proxy. Consequently, as data set 1 has no magnetic elements, I shall exclude it, deferring all further considerations of this to future research. This is a considerable problem because researchers are using this algorithm to identify robust features within the flow. If the algorithm will not pick out anything when using the temperature as the routine variable then what problems arise when using a proxy?

Before we can obtain results, we need to find the optimal values for the free parameters in the Fourier local correlation tracking routine. FLCT has three free parameters: the tolerance, the threshold and the Gaussian window size. When creating the reduced size images, the tolerance defines how far away from the maximum we wish to evaluate, and hence, the size of the reduced size images. The threshold considers if a pixel, (i,j) has moved far enough to calculate a velocity. If it has, a velocity is calculated, if not the velocity for that pixel is set to zero. The Gaussian window de-emphasises the area away from the flow structure we are considering. If α is too small then we may not encompass the full structure we are considering leading to innacurate results. Similarly, if α is too large then we may encompass more than one structure leading to incorrect results. The optimal values have been found by using images I_1 and I_2 for a quarter resolution.

I chose an optimal value of 0.5 for the tolerance as anything smaller ignored some significant values and anything larger increased computation time with no benefit. To find the optimal value for the threshold we use a trial and error method. I found that whenever the threshold was greater than 0.3 no pixels were considered in the creation of the velocity field. In Figure 5.1 the effects of varying the threshold are shown for depth $z = 0.2$. The field in the top left is the plot for a value of 0.1 and shows that the flow pattern is only just starting to emerge. If we lower the value of the threshold further to 0.01 we see that a granular pattern begins to emerge, as we would expect. A value of 0.001 shows a good estimation of the flow profile, emulating the behaviour of the solar photosphere qualitatively, where we see that the magnetic field accumulates preferentially at the boundaries. Lowering the threshold further increases the computational time massively but does not show any-

thing new in the flow profile. Hence, I have chosen a value of 0.001 for the threshold.

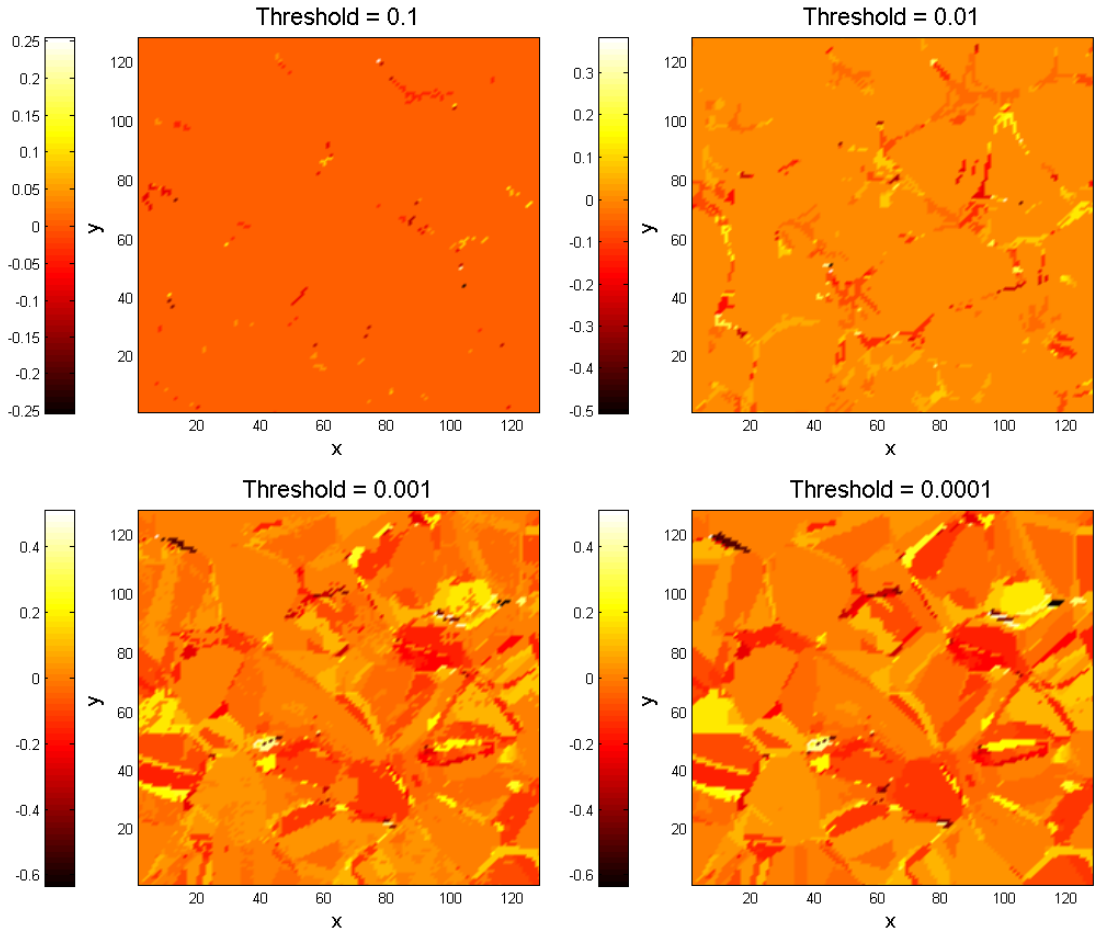

Figure 5.1: The flow profile at different thresholds between time 1 and time 2 for data set 2.

The final free parameter is the Gaussian window size, α. The results from the FLCT routine have some dependence on the choice of Gaussian window. Figure 5.2 illustrates this. When $\alpha = 5$, we see that the window is not big enough to encorporate some flow structures and the resulting velocity field shows smaller structures than what we would expect. We know that the result is not accurate as we can compare it with the velocities from the simulation. If we increase α to 10 the resulting flow profile looks more accurate, giving structures that are similar in size to what we would expect. By increasing the window size to 15, and then 20, the velocity field shows scales larger than expected. Hence, I have chosen a value of $\alpha = 10$. As resolution changes the value of this parameter, I will scale the parameter, accordingly. That is, if I halve the resolution then I will halve α. By observing Figure 5.2, it is clear to me that choosing the optimal value for α is not easy, and hence, there is room for error.

Finally, all these free parameters are sensitive to the cadance of the data. Smaller values of δt would probably produce more accurate results even for small α.

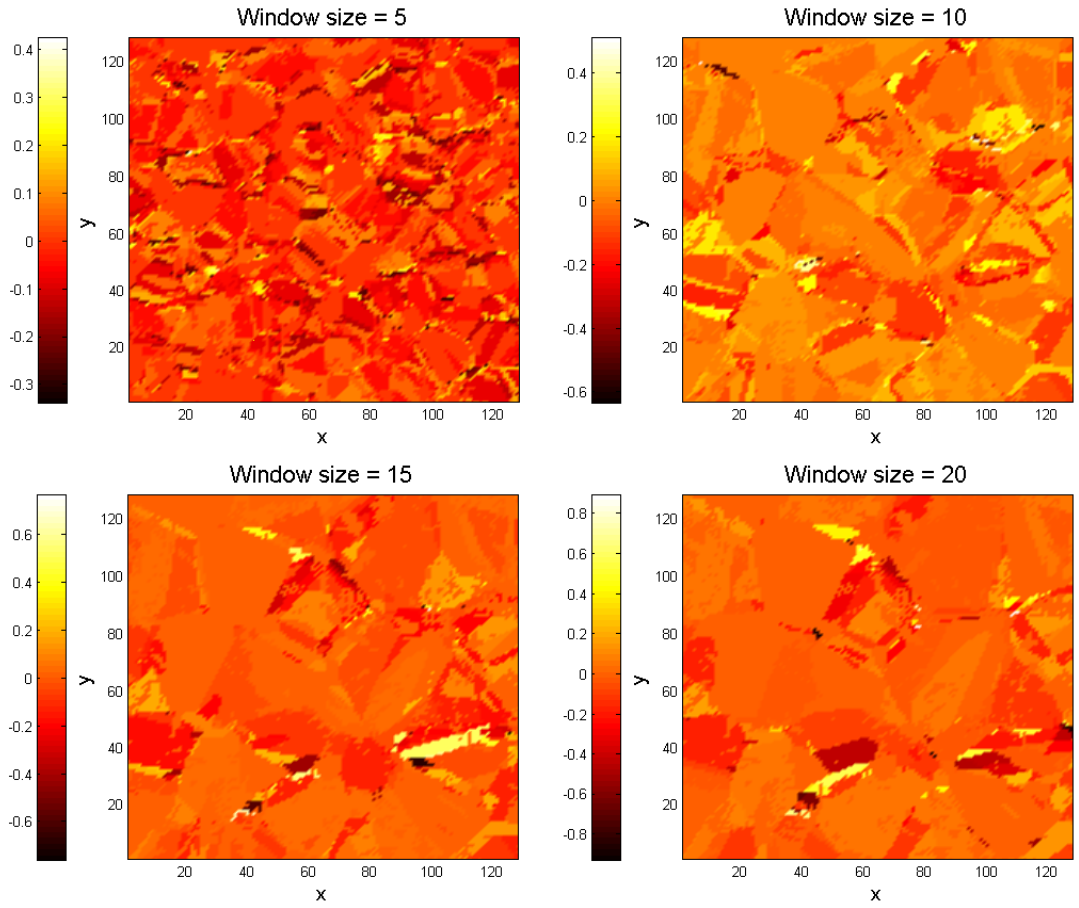

Figure 5.2: The velocity field for different Gaussian window sizes.

5.2 Results

Due to time constraints I could not run full resolution data. Therefore, I considered three cases: half resolution, quarter resolution, and an eighth resoltuion. The effects of resolution are shown in Figure 5.3. As we degrade the resolution it is apparent that the image becomes less constructed. The image in the top left is the full resolution of our simulation. For a typical solar observation, the resolution is similar to the image at the bottom right. It is clear that there is a massive difference between simulation and observational resolution, which could suggest why results differ. The analysis of resolution is quite important as it has been suggested that at certain resolutions correlation tracking is 'fruitless' (Bogart et al. 1988). It would be interesting to see if the same results can be found for simulation data.

I first ran the FLCT routine for times 1 and 2. In terms of results I found typical velocity scales of order unity for the half resolution and quarter resolution cases. This is in good agreement with what we would expect for a scale in the mesogranular range. The quarter resolution case gave a smaller velocity. Hence, only the two higher resolution cases compare favourably to real velocity data. I have plotted U_x and U_y for all cases in Figure 5.4. These plots clearly highlight why there are different results for velocities between resolution. The half and quarter resolution

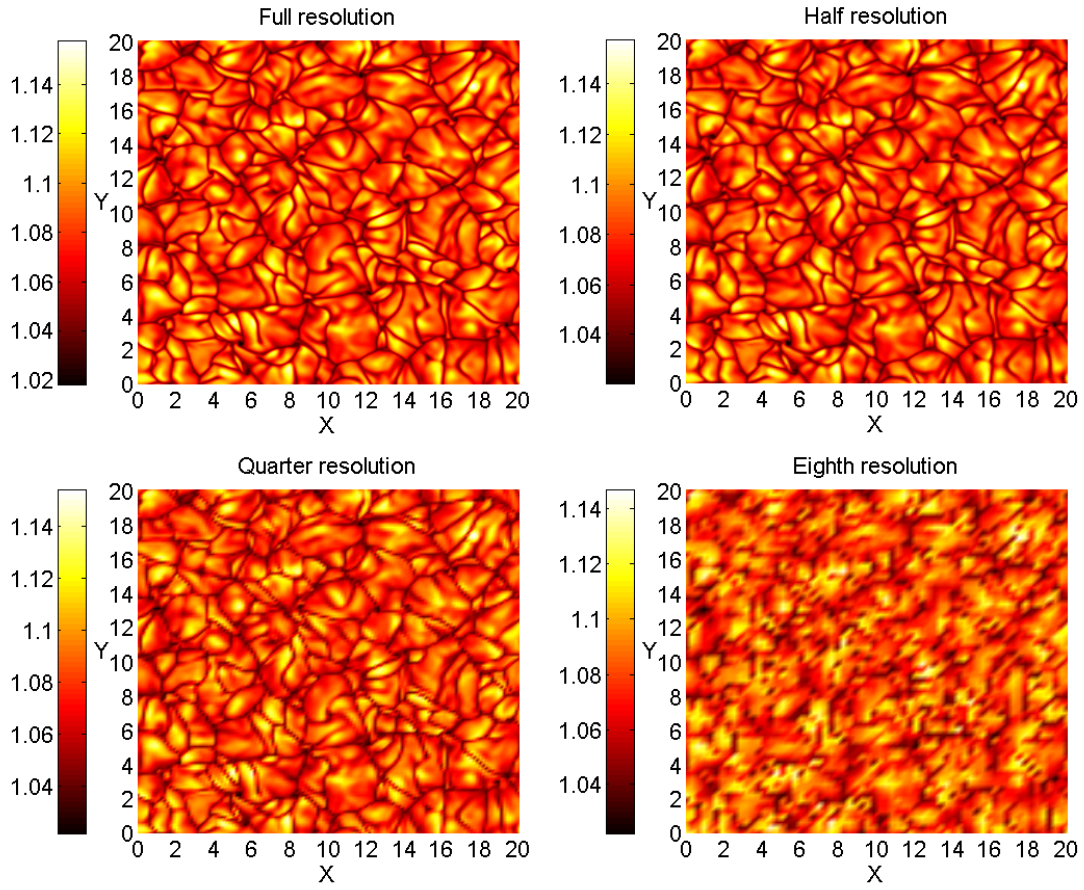

Figure 5.3: A plot showing different resolutions. The top left is the temperature map for our data at time 1 as shown in previous chapters. The top right image has been degraded by half, the bottom left by four and the bottom right by eight.

cases are very similar, so, it is unsurprising that the velocities obtained from both cases are similar. Furthermore, these plots show that the eighth resolution case is very different from the above two. This leads me to believe that when resolution is degraded far enough the results become innacurate.

To show whether or not FLCT was a good technique to observe mesogranulation I then plotted the kinetic energy spectrum for the above cases. The kinetic energy spectrum is different here than in Figure 3.1. In this case, it is purely an approximation as the velocity in the z-direction and the density have been neglected. Due to this fact, there will be changes in normalisation, but the overall shape should be similar. Because of these changes, I have only observed the kinetic energy spectrum at the top of the box, plotting the depth averaged kinetic energy spectrum for depths $z = 0.1, 0.2, 0.3$, in Figure 5.5. The graph at the top left shows the full resolution case depth averaged at the top of the box for comparison. In the half and quarter resolution cases there is a clear mesogranular peak, located at the same wave number as the full resolution case. However, the peaks are different shapes. Although this is expected due to the approximate nature of these spectra, there is some evidence that the results are dependent on resolution. In the lowest resolution case the kinetic energy spectrum is erratic and the peak is in a different location.

Furthermore, there is no evidence of mesogranulation for this case. There are hints of this shown in the relationship between the velocity and the resolution. As resolution decreases the velocity scales decrease. Therefore, it is unsurprising that there

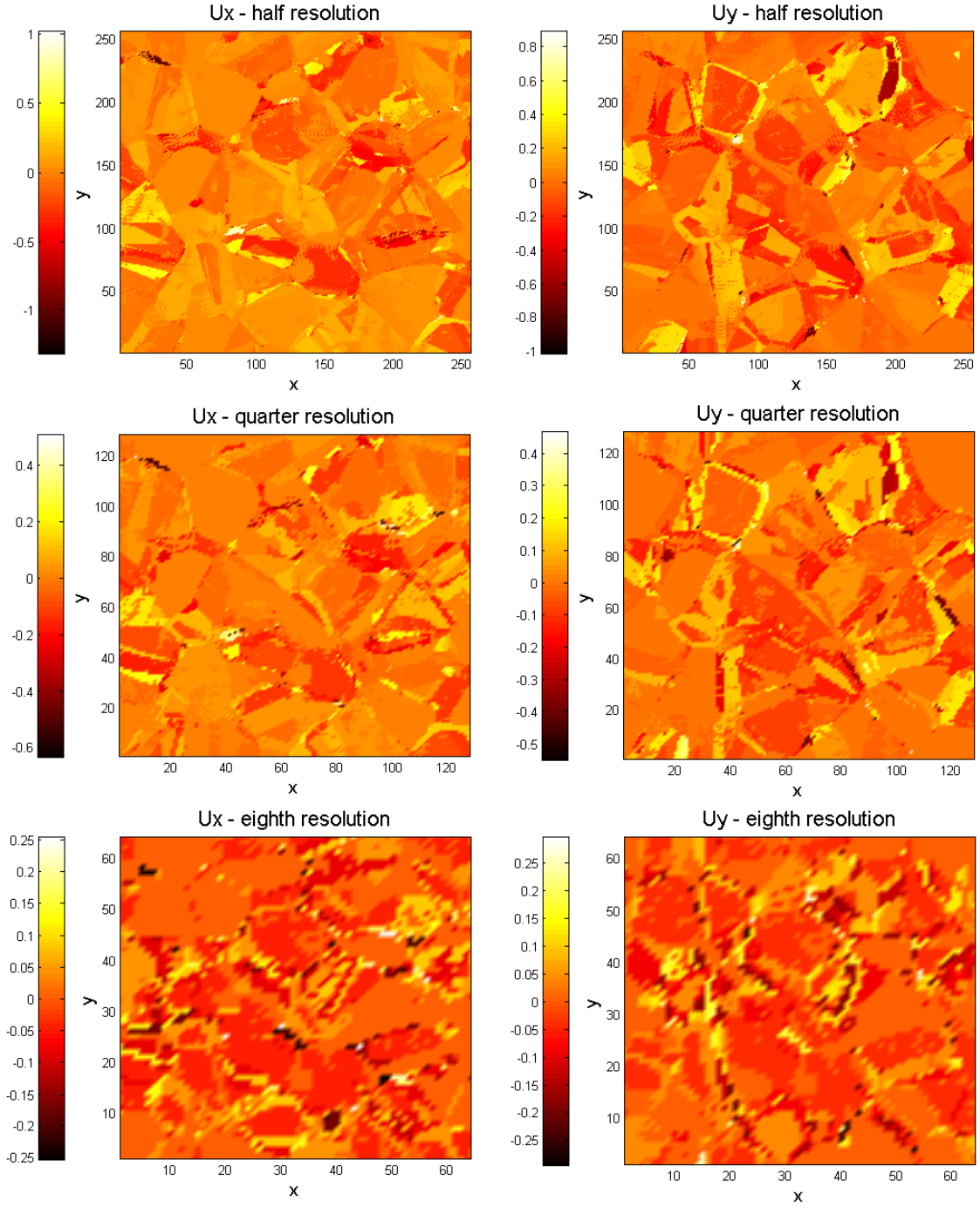

Figure 5.4: A plot of U_x and U_y for all three cases at times 1 and 2. Left: The plots for U_x. The bright patches are where the flow is moving to the right and the darker patches represent flows moving to the left. Right: The same plots, but for U_y. Brighter patches correspond to flows moving upwards and the darker patches are the flows moving downwards.

are differences between each case, and that when the resolution is lowered far enough mesogranular scales are not found.

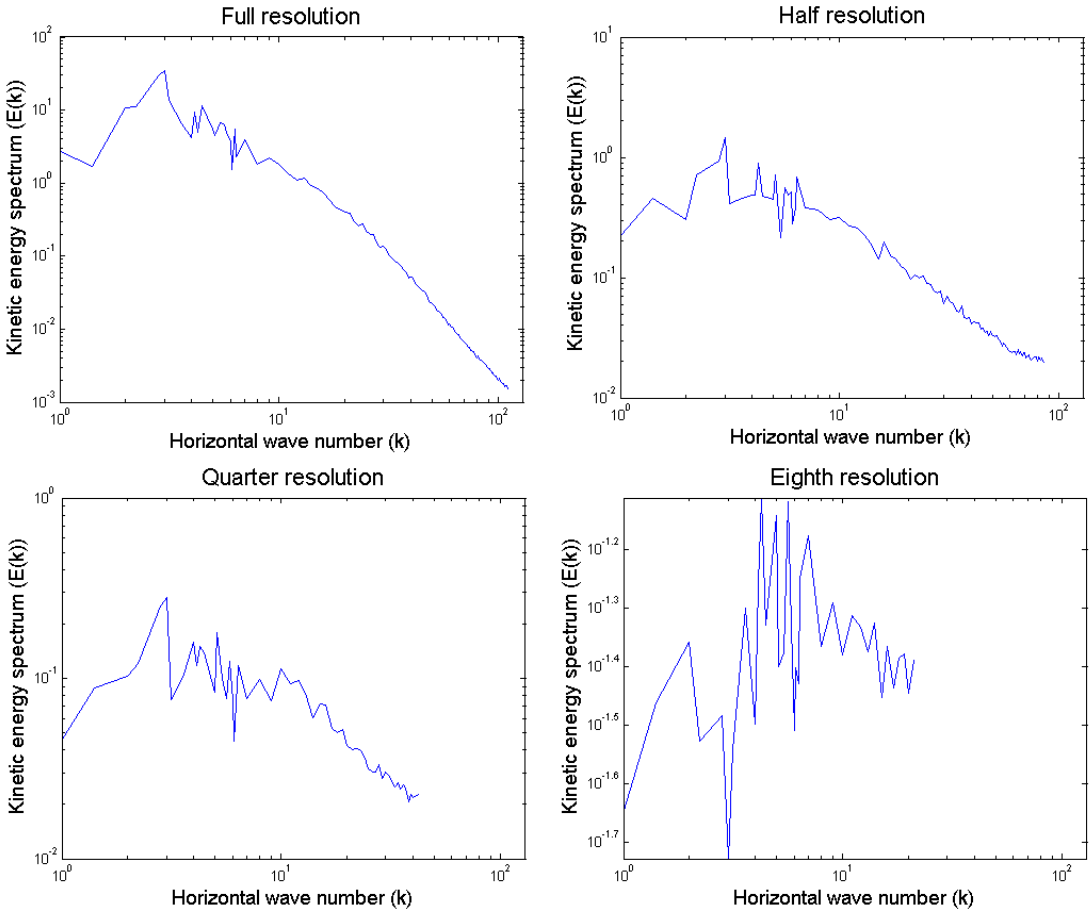

Figure 5.5: The depth averaged kinetic energy spectrum for a half, quarter and eighth resolution, respectively.

The only case that the FLCT routine could not pick out mesogranulation was the lowest resolution case. However, the above depth averaged spectrum was for times 1 and 2, only. This tells me that although mesogranulation is not present for the above case it may be present at other times. Hence, I have plotted the time averaged kinetic energy spectrum for the top of the box. Again, we see that there is no peak in the mesogranular range at any time. To add further validity to my results I then depth averaged the time averaged spectrum. This also showed that mesogranulation is not present. Hence, as we know mesogranulation exists in our simulation, there is very strong evidence that in low resolution studies the FLCT algorithm performs poorly.

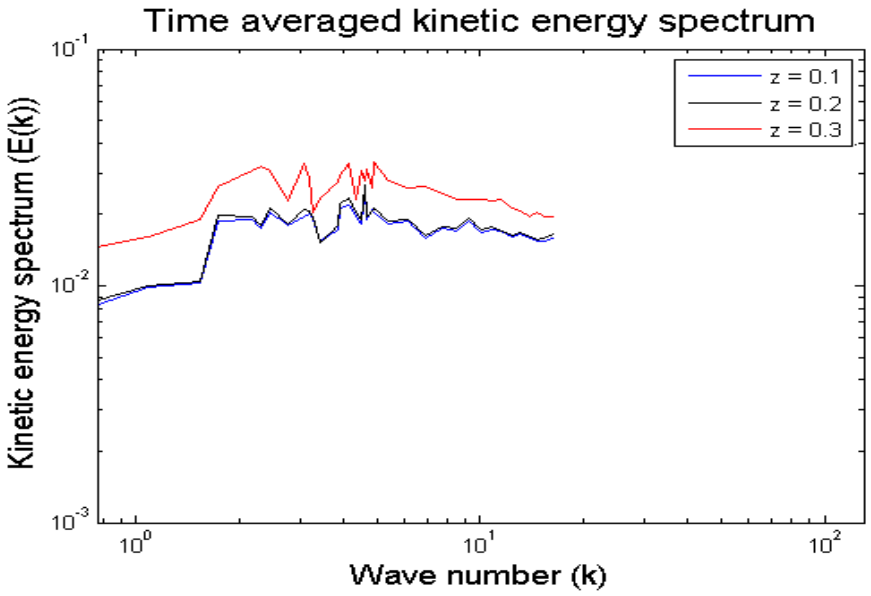

Figure 5.6: The time averaged kinetic energy spectrum for data set 2, at depths $z = 0.1, 0.2, 0.3$.

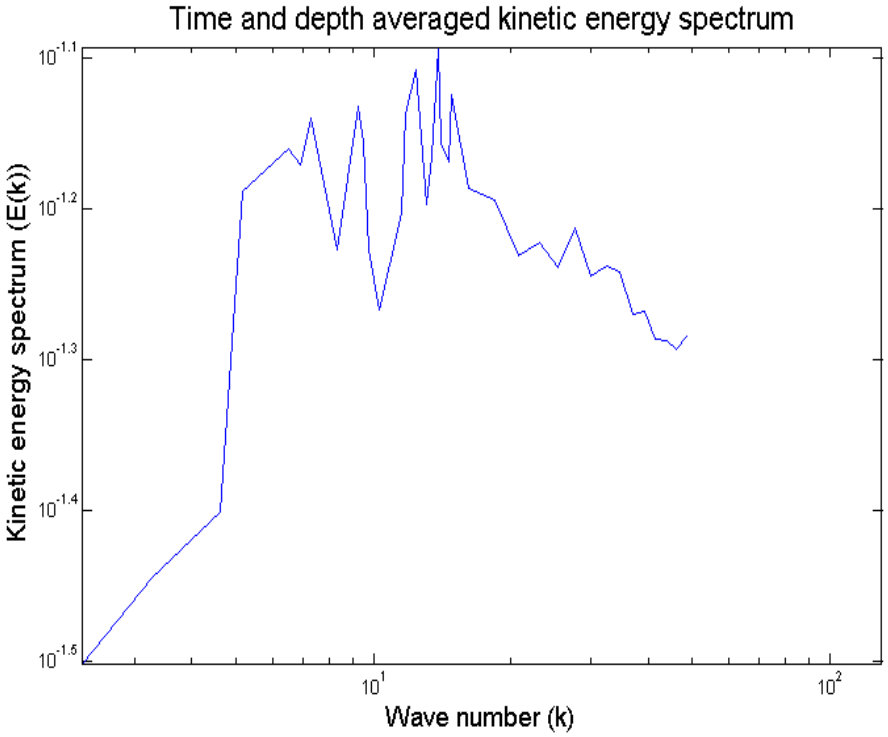

Figure 5.7: The time and depth averaged kinetic energy spectrum for data set 2.

6. Discussions, conclusions & future work

For this report, I introduced a compressible convection model and discussed how this could be related to the solar surface. Then, I calculated the kinetic energy spectrum showing that mesograulation was visible at all depths in the simulation. Furthermore, I implemented a Fourier local correaltion tracking algorithm on the simulation to see whether or not the algorithm was a good tool to study features at the solar surface.

In conclusion, this study may well have solved the mesogranulation puzzle. I found that the algorithm worked well and highlighted a mesogranular peak at high resolutions. This mesogranular pattern compares favourably with solar observations. However, when the resolution was lowered to that comparable with a typical solar observation, results showed that mesogranulation was not present in the simulation. It has been suggested that for observational studies higher order techniques like interpolation are necessary when reconstructing the velocity field (Welsch 2004; Rieutord 2007a). This opens an avenue to future researchers who could implement higher order techniques on the quarter resolution case to see if the results improve. Furthermore, higher cadence data may give better results. It may also, be beneficial to observe if different proxies give better results. Lastly, we have chosen to evaluate a variation of the most common algorithm. There are many other algorithms used by researchers that have not been validated.

In addition, there are still huge problems when working with 'idealised' models of this type. Many of the parameters in this model are massively different than what we would expect at the solar surface. For example, the magnetic Prandtl number is of order unity, whereas it should be much less than 1. This has not been investigated in convectively driven dynamos but is noteworthy because it has been shown that turbulent dynamos are inefficient for low Pm (Boldyrev & Catteneo 2004). The boundary conditions in this model are very idealised. That is, an impenetrable lower boundary is unrealistic for a model of the solar convection zone where the boundaries are open. Stein et al. (2003) suggested that dynamo action was inhibited when open boundary conditions were imposed at the bottom of the box. Brummell et al. (2010) came to the opposite conclusion with a two layer model of a convectively unstable region above a stable region. This suggests that the lower boundary being closed may not have as much of an effect as first thought, although, these are ideas that need further exploration. Additionally, more complex models will need to verify my results to increase the reliability of my work. Hence, this report should act as a stepping stone for future researchers.

Another avenue worth investigating is, that just because there is a peak in the kinetic energy spectrum at the mesogranular range, does not mean this is an intrinsic scale. It was suggested that mesogranulation could be the vertical component of supergranular convection (see, November 1994), or even, a more powerful extension of granulation (Strauss and Bonaccini 1997).

Bibliography

[1] Abdussamatov, H. I.: *The fine structure of solar granulation and its relationship to large-scale photospheric structures*, 1993: Astronomy & Astrophysics.

[2] Bogart, R. S., Ferguson, S. H., Scherrer, P. H., Tarbell, T. D., Title, A. M.: *On the feasibility of correlation tracking at moderate resolution*, 1988: Kluwer Academic Publishers.

[3] Boldyrev, S.; Cattaneo, F.: *Magnetic-field generation in Kolmogorov turbulence*, 2004: Physical Review Letters.

[4] Brummell, N. H., Hurlburt, N. E., Toomre, J.: *Turbulent Compressible Convection with Rotation. I. Flow Structure and Evolution*, 1996: The Astrophysical Journal.

[5] Brummell, N., Tobias, S., Cattaneo, F.: *Dynamo efficiency in compressible convective dynamos with and without penetration* 2010: The Astrophysical Journal.

[6] Bushby, P. J., Favier, B., Proctor, M. R. E., Weiss, N. O.: *Convectively-driven dynamo action in the quiet Sun*, 2011: Geophysical and Astrophysical Fluid Dynamics.

[7] Bushby, P. J., Favier, B.: *Mesogranulation and small-scale dynamo action in the quiet Sun*, 2014: Astronomy & Astrophysics.

[8] Cattaneo, F.: *On the origin of magnetic fields in the quiet photosphere*, 1999: The Astrophysical Journal.

[9] Cattaneo, F., Hughes, D. W.: *Solar dynamo theory: a new look at the origin of small-scale magnetic fields*, 2001: Astronomy & Geophysics.

[10] Cattaneo, F., Emonet, T., Weiss, N.: *On the Interaction between Convection and Magnetic Fields*, 2003: The Astrophysical Journal.

[11] Chou, D. Y., Labonte, B. J., Braun, D. C., Duvall, T. L., Jr.: *Power spectra of solar convection*, 1991: The Astrophysical Journal.

[12] Chou, D. Y., Chen, C. S., Ou, K. T., Wang, C. C.: *Power spectra of median- and small-scale solar convection*, 1992: The Astrophysical Journal.

[13] de Wijn, A. G., Rutten, R. J., Haverkamp, E. M. W. P., Sütterlin, P.: *DOT tomography of the solar atmosphere. IV. Magnetic patches in internetwork areas*, 2005: Astronomy and Astrophysics.

[14] Domínguez Cerdeña, I.: *Evidence of mesogranulation from magnetograms of the Sun*, 2003: Astronomy & Astrophysics.

[15] Fisher, G. H., Welsch, B. T.: *FLCT: A fast, efficient method for performing local correlation tracking*, 2008: ASP Conference Series.

[16] Ginet, G. P., Simon, G. W.: *On the evidence for mesogranules in solar power spectra*, 1992: The Astrophysical Journal.

[17] Lin, H., Rimmele, T.: *The granular magnetic fields of the quiet Sun*, 1999: The Astrophysical Journal.

[18] Louis, R. E., Ravindra, B., Georgoulis, M. K., Küker, M.: *Analysing the effects of apodizing windows on local correlation tracking using Nirvana simulations of convection*, 2015: Solar Physics.

[19] Matloch, L., Cameron, R., Schmitt, D., Schüssler, M.: *Modelling of solar mesogranulation*, 2009: Astronomy & Astrophysics.

[20] Matthews, P. C.; Proctor, M. R. E.; Weiss, N. O.: *Compressible magnetoconvection in three dimensions: planforms and nonlinear behaviour*, 1995: Journal of Fluid Mechanics.

[21] November, L. J., Toomre, J., Gebbie, K.B. and Simon, G.W.: *The detection of mesogranulation on the Sun*, 1981: The Astrophysical Journal.

[22] November, L. J.: *Inferring the depth extent of the horizontal supergranular flow*, 1994: Kluwer Academic Publishers.

[23] Ossendrijver, M.: *The solar dynamo*, 2003: The Astronomy and Astrophysics Review.

[24] Rieutord, M., Roudier, T., Malherbe, J. M., Rincon, F.: *On mesogranulation, network formation and supergranulation*, 2000: Astronomy & Astrophysics.

[25] Rieutord, M., Roudier, T., Roques, S., Ducottet, C.: *Tracking granules on the Sun's surface and reconstructing velocity fields. I. The CST algorithm*, 2007: Astronomy & Astrophysics.

[26] Rincon, F., Lignières, F., Rieutord, M.: *Mesoscale flows in large aspect ratio simulations of turbulent compressible convection*, 2005: Astronomy and Astrophysics.

[27] Roudier, T., Rieutord, M., Malherbe, J. M. & Vigneau, J.: *Determination of horizontal velocity fields at the Suns surface with high spatial and temporal resolution*, 1999b: Astronomy & Astrophysics.

[28] Stein, R. F., Nordlund, A.: *Solar small-scale magnetoconvection*, 2003: The Astrophysical Journal.

[29] Straus, Th., Deubner, F. L., Fleck, B.: *Is mesogranulation a distinct regime of convection?*, 1992: Astronomy & Astrophysics.

[30] Straus, Th., Bonaccini, D.: *Dynamics of the solar photosphere*, 1997: Astronomy & Astrophysics.

[31] Title, A. M., Tarbell, T. D., Topka, K. P., Ferguson, S. H., Shine, R. A.,: *Statistical properties of solar granulation derived from the SOUP instrument on Spacelab 2*, 1989: The Astrophysical Journal.

[32] Vögler, A., Schüssler, M.: *A solar surface dynamo*, 2007: Astronomy & Astrophysics.

[33] Wang, H.: *Do mesogranules exist?*, 1989: Kluwer Academic Publishers.

[34] Weiss, N. O.: *The Expulsion of Magnetic Flux by Eddies*, 1966: Proceedings of the Royal Society of London.

[35] Welsch, B. T., Fisher, G. H., Abbett, W. P.: *ILCT: Recovering photospheric velocities from magnetograms by combining the induction equation with local correlation tracking*, 2004: The Astrophysical Journal.

[36] Welsch, B. T., Abbett, W. P., De Rosa, M. L., Fisher, G. H., Georgoulis, M. K., Kusano, K., Longcope, D. W., Ravindra, B., Schuck, P. W.: *Tests and comparisons of velocity-inversion techniques*, 2007: The Astrophysical Journal.

[37] Yelles Chaouche, L., Moreno-Insertis, F., Martnez Pillet, V., Wiegelmann, T., Bonet, J. A., Knlker, M., Bellot Rubio, L. R., del Toro Iniesta, J. C., Barthol, P., Gandorfer, A.: *Mesogranulation and the solar surface magnetic field distribution*, 2011: The Astrophysical Journal Letters.